Isolated Bidirectional DC-DC Converter and System Level Control for EV Charger

Jiantong Zhang

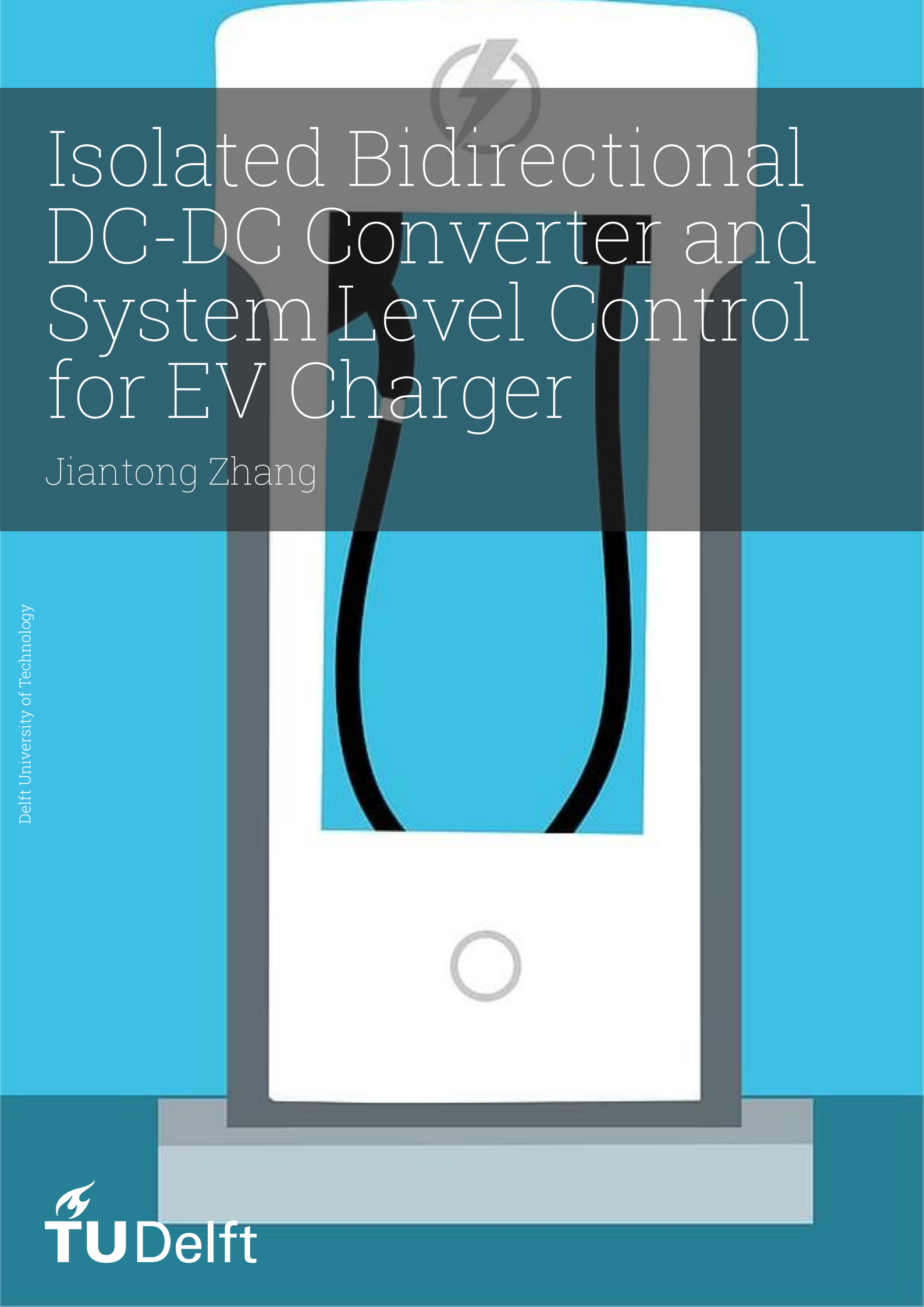

Delft University of Technology

TU Delft

Isolated Bidirectional DC-DC Converter and System Level Control for EV Charger

by

Jiantong Zhang

in partial fulfillment of the requirements for the degree of

Master of Science
in Electrical Power Engineering

at the Delft University of Technology,
to be defended publicly on Monday August 28,2023 at 09:00 AM.

Supervisor:	Dr. Zian Qin	TU Delft
	Dr. Ir. Laurens Mackay	DC Opportunities R&DBV
Thesis Committee:	Prof. Dr. Ir. Pavol Bauer	TU Delft
	Dr. Zian Qin	TU Delft
	Dr. Aleksandra Lekic	TU Delft
	Dr. Ir. Laurens Mackay	DC Opportunities R&D BV
Company Supervisor:	Ir. Jesse Echeverry,	DC Opportunities R&D BV

TU Delft Delft University of Technology

DC pportunities

Abstract

Jiantong Zhang
Delft, August 2023

This thesis presents the design of an isolated bidirectional DC-DC converter for a dual-output electric vehicle (EV) charger. The central objective of this study is to select a topology capable of facilitating bidirectional power flow and enabling car-to-car charging. Simultaneously, the aim is to devise a simple control scheme suitable for managing a wide range of output voltages with connections to a bipolar DC grid as input.

In the process of topology selection, a comprehensive literature review is conducted to assess various converter topologies. To discern the suitable topology, an in-depth evaluation is undertaken, wherein the multiport CLLC converter and the Triple Active Bridge converter are simulated in PLECS and their performances are compared based on different operation modes and bidirectionality. This comparative analysis aids in identifying the most appropriate topology for the intended application.

Subsequently, in pursuit of maintaining simple control for the EV charger with the chosen Multiport CLLC converter, an investigation into the interleaved buck converter is carried out. Different topologies are compared based on the cost and efficiency, including different numbers of legs for the buck converter and different numbers of inductor cores used for the converter. The application of a cascade proportional-integral (PI) control strategy is explored to regulate voltage.

Upon the culmination of the topology selection and the development of the interleaved buck converter, a comprehensive system-level control strategy is introduced. Diverse operational modes are outlined, and several simulations are modelled across various scenarios to validate the proposed approach's adaptability.

In conclusion, this study delves into the detailed design of an isolated bidirectional DC-DC converter tailored to a dual-output EV charger. By systematically assessing topologies, investigating control strategies, and performing thorough simulations, this research contributes to advancing the field of EV charging technology.

Acknowledgement

As I complete this master's thesis, I would like to extend my sincere gratitude to everyone who has supported and guided me along the way.

First and foremost, I am immensely thankful to my supervisor, Dr. Laurens Mackay from DC Opportunities and Dr. Zian Qin from TU Delft, for their unwavering support, invaluable insights, and continuous encouragement. Their guidance has been instrumental in shaping the direction of this research and in pushing me to strive for excellence. A special thanks is due to my daily supervisor, Ir Jesse Echeverry, who has supported me in my daily work and offered me kind assistance throughout. His guidance has been instrumental in helping me grow and develop professionally. I am grateful for his encouragement and the insight he provided to help me succeed. I could not have asked for a better supervisor.

I am also grateful to all the employees of DC Opportunities B.V. for their dedication to imparting knowledge and for fostering an environment of learning and growth. In addition, I would like to thank the master students at DCO for discussing each other's projects and offering assistance.

I extend my appreciation to my family for their patience, understanding, and belief in me. Their encouragement and moral support have been my driving force during the challenging times of this academic endeavour. Having two years in the Netherlands has been an unforgettable experience for me, and I owe my parents a huge thank you for providing me with financial support.

My sincere gratitude goes out to my friends who have been unwavering pillars of support throughout my master's thesis preparation. They have played an important role in shaping the outcome of this research through their encouragement, insightful discussions, and empathetic understanding.

Last but not least, I want to thank myself. For the past two years, I have the ability to regulate myself has kept me mentally stable throughout all the challenges and stress I have encountered.

It has been an inspiring journey of discovery and learning culminating in the completion of this thesis. My gratitude goes out to the people who have been a part of this journey and for the opportunities I've been given.

Contents

List of Figures

List of Tables

Nomenclature

Abbreviations

Definition	Abbreviation
Electric Vehicle	EV
Battery Electric Vehicle	BEV
Electric Vehicles Initiative	EVI
Plug-In Hybrid Electric Vehicles	PHEV
Advanced Power System	APS
Direct Current	DC
Alternating Current	AC
State of Charge	SoC
Triple Active Bridge	TAB
Dual Active Bridge	DAB
Zero Voltage Switching	ZVS
Solid-State Transformer	SST
Isolated Bidirectional DC/DC Converter	IBDC
Multiport Converter	MPC
Multi-Input Multi-Output	MIMO
Single-Input Single-Output	SISO
Single-Input Dual-Output	SIDO
Generalized Average Modelling	GAM
Generalized Harmonic Approximation	GHA
Proportional Integral	PI

Symbols

Symbol	Definition	Unit
$PI_v(s)$	Voltage loop regulator	
$PI_i(s)$	Current loop regulator	
$Gvd(s)$	Voltage to duty cycle transfer function	
$Gid(s)$	Current to duty cycle transfer function	
$V_o(s)$	Output Voltage of the EV charger	[V]
$I_o(s)$	Output Current of the EV charger	[A]
$d(s)$	Duty cycle of the interleaved buck converter	
n	Transformer turns ratio	
f_s	Switching frequency	[Hz]
P_{12}	Power transferred for DAB	[W]
V_1	Voltage across the primary side of the transformer	[V]
V_2	Voltage across the secondary side of the transformer	[A]
L	DAB inductance	[H]
V_o	Output Voltage	[V]
V_{in}	Input Voltage	[V]
P_1	Input Power of TAB	[W]
P_2	Output Power on the secondary port of TAB	[W]
P_3	Output Power on the tertiary port of TAB	[W]
L_{rp}	Primary side resonant inductance of CLLC converter	[H]

Symbol	Definition	Unit
L_{rs}	Secondary side resonant inductance of CLLC converter	[H]
L_{rt}	Tertiary side resonant inductance of CLLC converter	[H]
C_{rp}	Primary side resonant capacitance of CLLC converter	[F]
C_{rs}	Secondary side resonant capacitance of CLLC converter	[F]
C_{rt}	Teritiary side resonant capacitance of CLLC converter	[F]
L_m	Magnetic Inductance of the transformer	[H]
Z_r	Resonant tank impedance	[Ω]
R_{AC}	Effective AC load	[Ω]
R_{DC}	Effective DC load	[Ω]
f_r	Resonant Frequency of CLLC converter	[Hz]
L_{eq}	Equivalent inductance of multiport CLLC converter	[H]
N_1	Number of turns on the primary side of the transformer	
N_2	Number of turns on the secondary side of the transformer	
N_3	Number of turns on the tertiary side of the transformer	
D	Duty cycle of interleaved buck converter	
L_1	Inductor of interleaved buck converter	[H]
L_2	Inductor of interleaved buck converter	[H]
T_s	Switching period of interleaved buck converter	[s]
V_{pole}	Grid pole voltage	[V]
ϕ	Phase shift for DAB and TAB	[rad/s]

1 Introduction

As part of this chapter, background information about the project will be presented, including the benefits of DC microgrids and recent developments in the electric vehicle (EV) market. The problem that will be solved by this project will also be defined and discussed. Furthermore, the outline of this project, as well as the research questions, will be presented.

1.1. Background

1.1.1. DC Microgrid

In recent years, renewable energy sources have increased interest in DC microgrids, particularly in relation to electronic loads and electrified vehicles (EVs) in modern power networks [1]. The increased adoption of renewable energy systems has prompted the utilization of microgrids as an effective approach for integrating distributed generation [2]. Additionally, improvements in power electronics technology have resulted in increasing DC loads and power converters for various DC applications over the years.

DC distribution offers several advantages over traditional AC grids, including easier control, a more straightforward interface for renewable energy sources, as well as electronic loads and energy storage capacity [3]. In addition to these benefits, there would be a significant increase in dc loads, including LED lights, laptop computers, and electric vehicle chargers, which could make DC distribution attractive as a viable solution to address future energy needs. Additionally, by implementing effective energy management and control strategies, it is possible to secure a reliable power supply with less fluctuations in voltage, as well as to ensure a reliable energy dispatch between the power source and the loads [2]. Fig. 1.1 illustrates the integration of battery electric vehicles (BEVs) and renewable energy sources within microgrids, enabling the direct provision of high DC power without the need for reactive power compensation. In this DC microgrid configuration, the utility grid and PV panels serve as the primary power sources. All sources and loads are connected through the DC Bus, and by connecting with different DC-DC converters, the EV and battery could be charged and discharged properly. Under certain situations, the storage battery and the battery inside an electric vehicle could be served as power sources for to feedback the grid due to economic considerations. By effectively managing the generated power from the PV panels and controlling the power flow between the microgrid and charging terminals based on demand, the charging station's power conversion efficiency can be significantly enhanced [4].

1.1.2. Recent EV Chargers in the Market

As a result of environmental concerns, the world is gradually shifting away from the use of fossil fuels due to global warming, and electric vehicles are one of the most promising solutions to this problem. Electric vehicles play a pivotal role in the decarbonization of road transport, addressing a significant contributor to global emissions, as the sector accounts for approximately 16% of total emissions [5]. In 2010, the Clean Energy Ministerial (CEM) established a multi-governmental policy forum called Electric Vehicles Initiative (EVI). In order to accelerate the adoption of EVs worldwide, EVI brings together

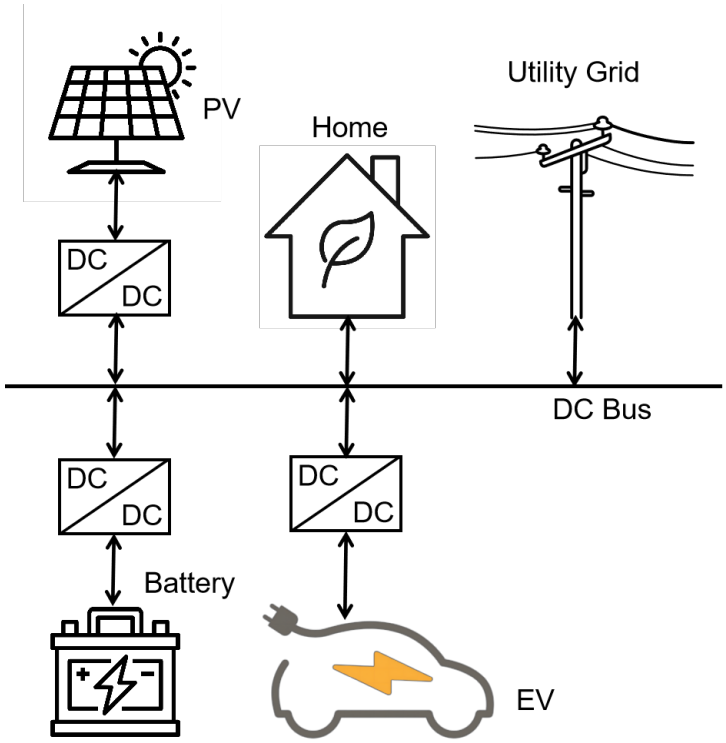

Figure 1.1: Typical DC Microgrid

government policymakers and a variety of partners twice a year to share knowledge and support EV development [6]. Despite slowdowns in the supply chain and the continuing pandemic of Covid-19, 2021 saw record electric car sales as a result of government assistance and consumer demand. As shown in Fig 1.2, electric vehicles have tripled in three years to reach over 16.5 million.

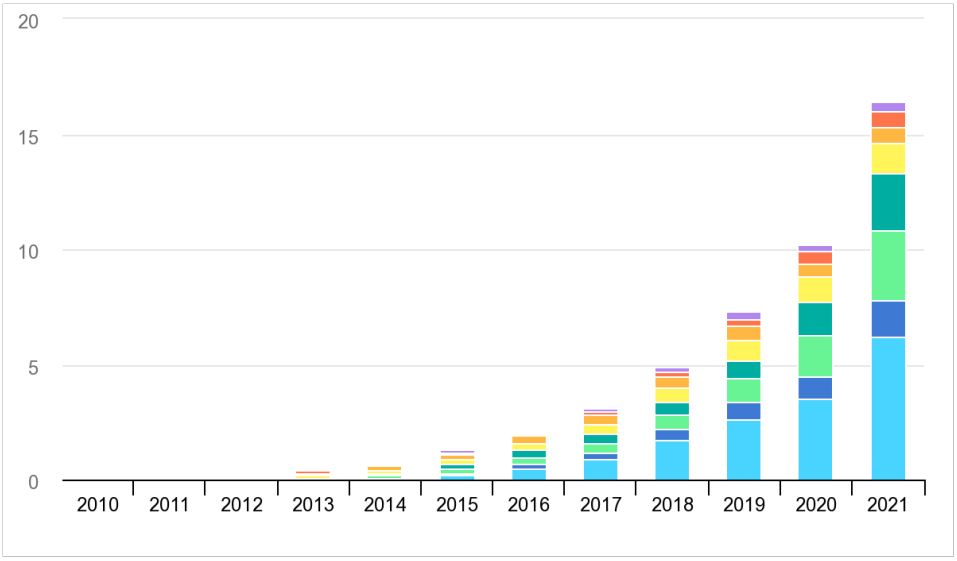

Figure 1.2: Global Electric Vehicle Stock, 2021-2021[**IEA**]

Fig 1.3 shows that electric car sales are accelerating and the EV markets are expanding quickly. As a result of several years of relative stagnation, China's sales tripled to 3.3 million units in comparison with 2020, followed by Europe at 2.3 million units, up two-thirds from last year [5]. As the sales increased, the available electric car models reached above 450 in 2021, more than double the number available

in 2018. As a result, automakers are producing new options quickly to appeal to a broader market and capture the EV market share. Meanwhile, because the driving range is still a concern for consumers buying EVs, the driving range slowly increased over the 2015-2021 period. For battery electric vehicles (BEVs), the average range reaches 349km, and plug-in hybrid electric vehicles (PHEVs) could drive to 62km, exceeding 60km for the first time in 2021 [5]. The increasing driving range relies heavily on the battery voltage range and sizes.

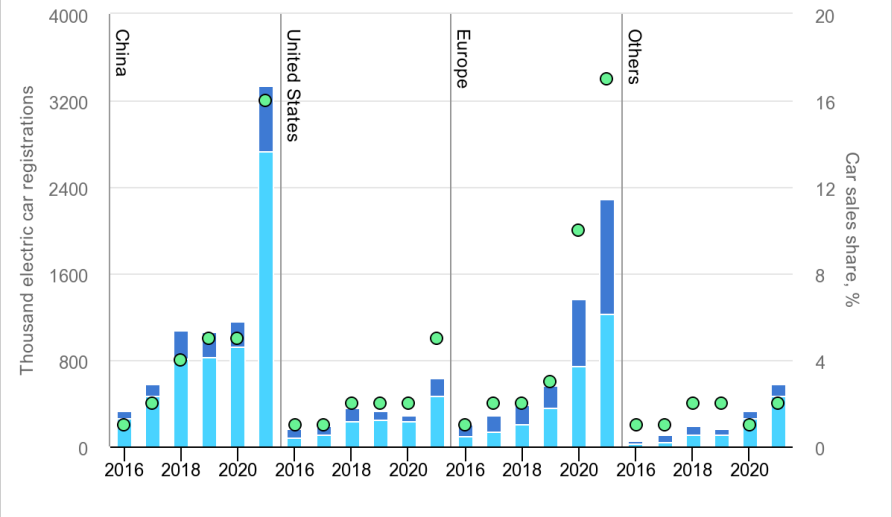

Figure 1.3: Electric car registrations and sales shares, 2016-2021, in China, the US, Europe, and other regions [5]

1.2. Problem Definition

1.2.1. EV Charger Requirements

As introduced in Section 1.1.2, the growing EV market requires an increasing EV battery size and an increase in the EV chargers. Worldwide, 1.8 million charging points are publicly accessible, of which a third are fast chargers, according to [6]. This number increased by 37% in 2021 but was dragged behind due to the pandemic compared with the growth rate in 2020 (45%). As mentioned before, China plays a lead role in the EV sector, the number of installed slow chargers has grown by 35 % to around 680,000 units available to the public in 2021, as shown in Fig. 1.4. But the growth rate was much slower than in previous years due to the COVID-19 pandemic.

Compared to slow charging, fast charging (with a power rating exceeding 22 kW) is experiencing a more rapid deployment in China. In fact, over 40% of public charging stations now offer fast charging, indicating an accelerating demand for fast charging stations [6]. However, [6] points out that as EV stocks grow, the ratio of charging points per EV drops. Interestingly, the data reveals that countries that are heavily reliant on public charging witness a proportional expansion of their charging networks. Furthermore, countries with a high residential charger prevalence, as compared to those with a low prevalence, require fewer public chargers in order to accommodate a greater number of electric vehicles. In the Netherlands, the share of fast chargers remains really low due primarily to the wide deployment of slow chargers by the government. There is a strong likelihood that public charging stations will continue to become more and more relevant in the EV market as a result.

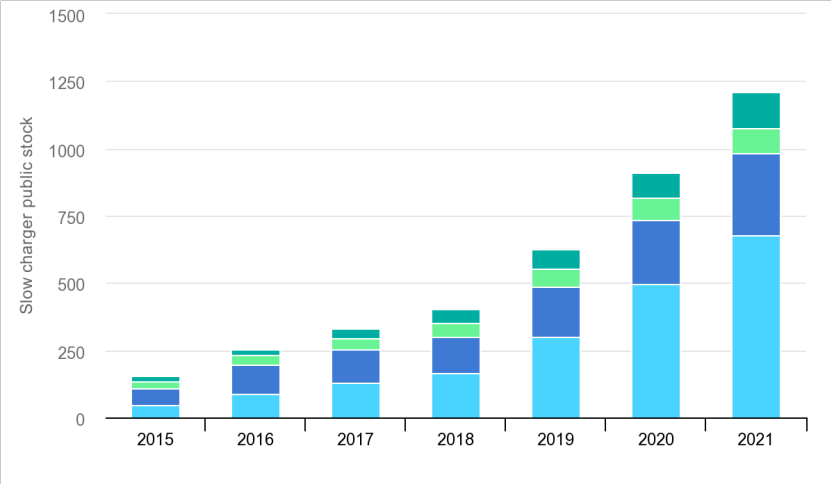

Figure 1.4: Slow Publicly Available Chargers, 2015-2021 [7]

1.2.2. Smooth Integration to Existing Public Lighting Infrastructure

It is true that plug-in hybrid electric vehicles (PHEVs) and plug-in electric vehicles (PEVs) offer numerous advantages over their gasoline-powered counterparts. Still, the adoption of electric vehicles is hindered by a number of obstacles. For adopting electric vehicles, the lack of proper charging stations and the impact brought by the existing charging stations on the electric grid such as fluctuations, voltage outages and harmonics, becomes the main obstacles that limit the adoption of EVs [2]. Moreover, electric vehicles introduce an additional burden to the existing grid, particularly during peak hours.

The optimal quantity of chargers per electric vehicle (EV) will vary based on regional factors such as the availability of housing, the average distance travelled, population density, and the extent to which home charging is prevalent. While home and workplace charging are expected to fulfil a significant portion of the charging demand, it is necessary to significantly increase the number of public chargers, reaching over 15 million units by 2030. This expansion, amounting to a ninefold increase, is crucial to meet the anticipated requirements outlined in the APS (Advanced Power System) and ensure consumers have sufficient and convenient charging coverage [6]. As said in Section 1.1.2, there are various modes of electric vehicle chargers available in countries worldwide, however, as electric vehicles consume a large amount of electricity, charging them can create additional burdens and unwanted peak load demands on the distribution grid [2]. That's one of the reasons for designing this EV charger that brings low impact to the connected DC microgrid.

1.2.3. EV Charger Overview

In summary, due to the rapid growth of the electric vehicle (EV) market, there is a rising demand for EV chargers. Therefore, there is a need for the development of slow chargers that have minimal impact on the power grid. These chargers should be designed in a way that ensures their operation does not heavily strain the grid infrastructure. In a level 3 electric vehicle charger, batteries ranging from 200V to 920V can be charged with a DC line connected between the battery and the charger to reduce charging time [8]. The Terra DC EV chargers from ABB (Terra 94/124/184) have an output voltage of up to 920V DC, which is suitable for any EV battery. This led to the purpose of this project: designing an isolated bidirectional DC-DC converter with a wide output voltage range for EV chargers and designing a system-level control for this converter.

Fig. 1.5 shows the overview schematic of this EV charger. By connecting to the bipolar DC microgrid where the neutral line is used for grounding, it has the ability to charge two cars at the same time. The grid will provide an input voltage ranging from 640 V to 760 V. An isolated bidirectional converter connected to the grid will produce an output voltage of around 1000 V. There are two potential topologies of the isolated bidirectional converter which could deliver 5.5 kW each. There are two potential options to consider. The first option involves using two identical converters connected to the grid. This approach offers the advantage of reducing control complexity. Alternatively, the second option is to utilize a single dual-output converter, which can help save four switches on the primary side. Each option presents its

own set of benefits, and the choice between them depends on factors such as system requirements, cost considerations, and overall design objectives. A detailed comparison of these two options will be discussed in the following chapters. At the output of the isolated converter, two identical interleaved buck converters are connected to the corresponding output port in order to support a wide output voltage range in order to charge all different types of EVs with a wide voltage range of EV batteries. Typically, by the fast-developing EV battery sizes, this converter is designed to charge EVs ranging from 200 V to 920 V.

In addition, the concept of inverse power flow is taken into account, particularly when considering the scenario of supplying power from the battery back to the grid. This consideration is driven by economic factors, as it allows for potential benefits and opportunities in terms of cost savings and optimizing energy utilization. By enabling bidirectional power flow, the system can leverage the battery as a valuable resource to support grid stability and potentially participate in energy markets, contributing to a more economically efficient energy ecosystem. Furthermore, car-to-car charging will be thoroughly examined and devised as part of the investigation. In certain situations, such as when three cars have a battery state of charge (SoC) of 33% each, it may be more advantageous to utilize the power from two cars to charge one vehicle to 100%, all without relying on power exchange with the grid. This approach explores the potential for efficient energy sharing between electric vehicles, maximizing the utilization of available resources and minimizing the reliance on external power sources.

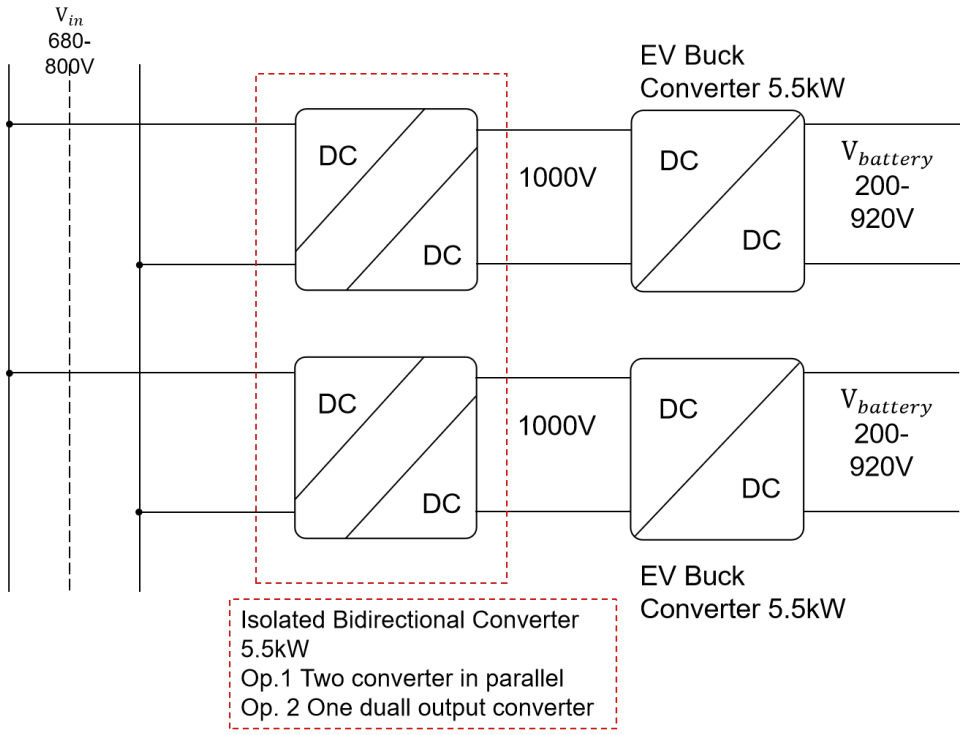

Figure 1.5: Dual Output EV Charger Converter Illustration

1.3. Research Questions

Below are the three research questions for this project that came up from the problem definition mentioned in the above section.

1. What are the suitable topologies for a bidirectional isolated dual-output EV charger connected between a DC microgrid and considering a wide output voltage range of EV batteries?

   (a) What is the outcome of a comparative analysis between the Triple Active Bridge and Multiport CLLC converter for the dual-output EV charger converter application?

2. How can a simplified open-loop control strategy be implemented for the CLLC while maintaining ZVS over the entire input voltage range of the DC grid?

3. How to model and design the control for the EV charger converter and simulate the control across various scenarios, including load changes, power flow changes, and grid variations?

1.4. Outline

The following list provides a brief overview of each chapter's content, which is divided into six chapters.

- Chapter 1: Introduction
  - Provides the background information of this project, including DC microgrids and EV charger market and defines the problem of the project. Additionally, the research questions of the project are presented.
- Chapter 2: Literature Review
  - Provides different DC-DC converter topologies that could be used in this project and compares the pros and cons of these converters. Furthermore, the methodology and control methods of the interleaved buck converter are elaborated.
- Chapter 3: System Design and Comparison
  - Mainly compares two different dual-output converter topologies based on their performances and simulation results. Meanwhile, some further research such as DC-blocking capacitors and decoupled control are also included in this chapter
- Chapter 4: System Modelling and Control
  - Provides the complete control design of the whole system, including the constant frequency control of the multiport CLLC resonant converter and the double loop control of the interleaved buck converter.
- Chapter 5: Simulation Results and Analysis of the System Level Control
  - Provides the simulation results of the system level control under different control scenarios. And the results will be analysed and discussed in this chapter.
- Chapter 6: Conclusion
  - Answers the research questions of this project and provides conclusions of the project and some recommendations for future work.

2

Literature Review

2.1. Topology Comparison

DC-DC converters can be classified into two main categories: non-isolated and isolated converters. Figure 2.1 shows the converter classification based on the two categories. The main difference is that a high-frequency transformer separates the input from the output port and provides electrical isolation [9]. As examples of non-isolated DC-DC converters, Buck, Boost, Buck-Boost, and Modular Converters are listed. An interleaved buck converter is another type of buck converter, and a modular converter includes both a multimodule converter and a multilevel modular converter.

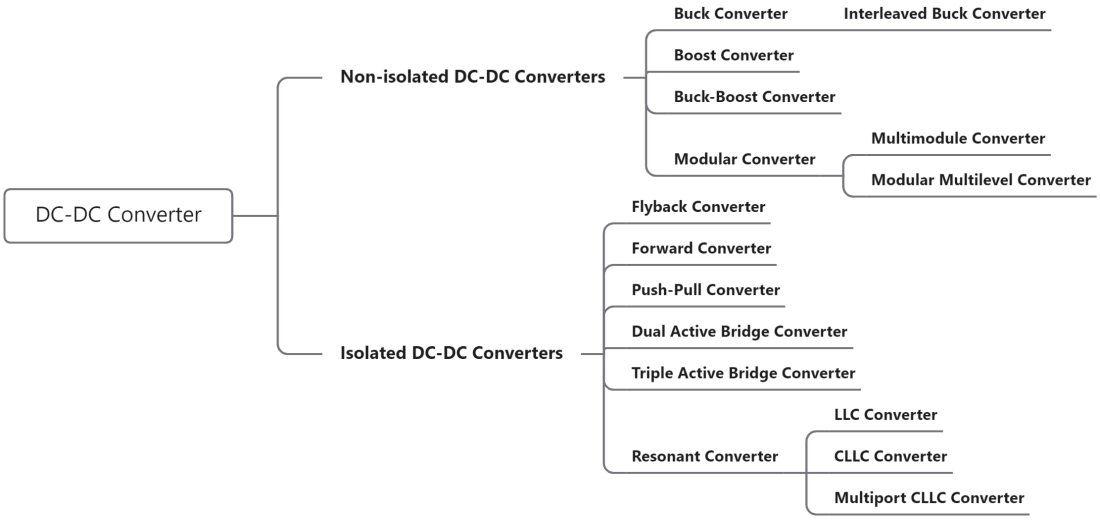

Figure 2.1: DC-DC Converters Classification

Galvanic isolation is usually required for specific applications such as electric vehicle charging in order to ensure safety considerations. A multiwinding high-frequency transformer is used to achieve this galvanic isolation. It assumes a significant role in facilitating isolation between the grid and load sides of power the converters. Specifically, this isolation mechanism establishes a barrier between the primary and secondary sides of the converter, effectively impeding the transfer of electrical energy and signals. Through galvanic isolation, potential risks, such as electrical hazards and disturbances, are mitigated as they are prevented from permeating between the two sides of the system. Consequently, galvanic isolation plays a vital role in enhancing the safety and reliability of power electronic systems by ensuring the isolation and containment of electrical phenomena within their respective domains.

2.1.1. Single Output Isolated DC-DC Converter

Enssential DC-DC Converter Comparison

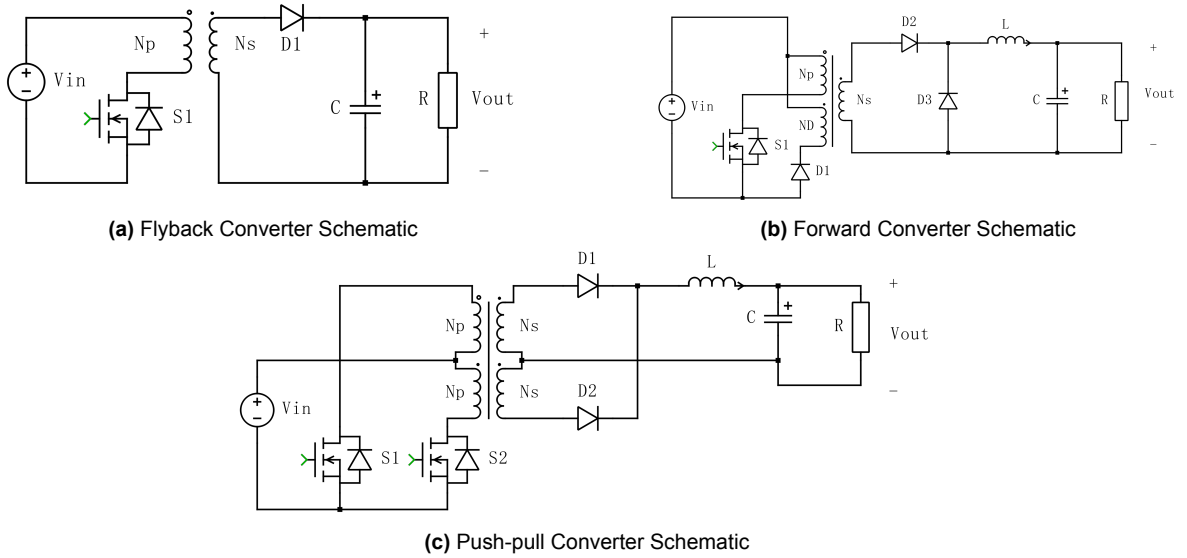

(a) Flyback Converter Schematic

(b) Forward Converter Schematic

(c) Push-pull Converter Schematic

Figure 2.2: Three Different Types of Single-output DC-DC Converter

Three types of basic single-output converters were compared and their schematics are shown above, including flyback converter (Fig.2.2a), forward converter (Fig.2.2b) and push-pull converter (Fig.2.2c). Various medium-voltage DC-DC converter topologies for electric bus fast charging stations are compared in [10]. Due to their high ripple currents, flyback converters require additional capacitors when used in low-power applications. Typically, forward converters are used in medium power applications due to their single-ended classification, but they have a limited duty cycle and poor transformer utilization. High-power push-pull converters have a really high voltage stress across the switches on the primary side despite getting full utilization of the transformer with a wide duty cycle range.

Besides the three types of DC-DC converters introduced above, the other three topologies are also investigated due to the high utilization of the transformer and high efficiency. The literature review of the three converters is shown below.

LLC Resonant Converter

Recently, soft-switching resonant topologies have been gaining increasing market interest. In order to enhance comprehensive power conversion efficiency, an LLC resonant converter, combining the soft-switching characteristics of the ZVS for primary power switches and soft commutation for output rectifiers, has been proposed and investigated [11]. Fig.2.3 shows the basic schematic of the LLC resonant converter. However, the LLC converter can only operate unidirectional power conversion, so it doesn't meet the design requirement of the EV charger [12]. [13] and [9] also show that due to the large RMS currents on both sides, LLC is not suitable for reverse power transmission. Fig.2.4 shows the typical voltage gain curves of the resonant tank in terms of normalized frequency. The converter could achieve Zero-Voltage-Switching (ZVS) when it operates with an inductive impedance of the resonant tank, which means that the current lags the voltage through the tank. Similarly, the resonant tank impedance may become capacitive when output power increases, and so ZVS may be lost.

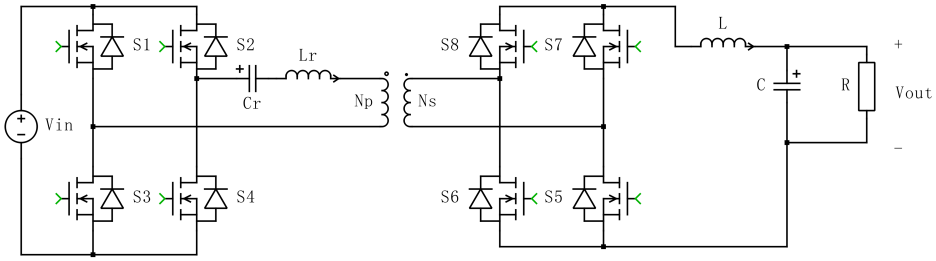

Figure 2.3: LLC Resonant Converter Schematic

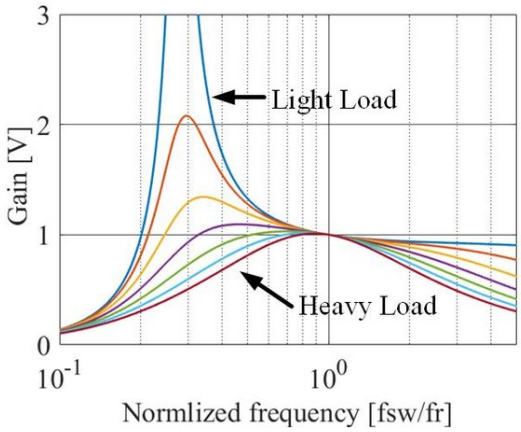

Figure 2.4: DC gain response of LLC resonant tank [14]

CLLC Resonant Converter and Dual Active Bridge (DAB) comparison

Using the CLLC resonant converter in EV chargers and DC microgrids has significant potential, as it can transfer power in both directions, the same as the DAB converter, with its ease of implementation of soft-switching, bidirectional power flow capability, and symmetrical design. Fig.2.5 shows the basic schematic of the CLLC resonant converter and Fig.2.6 shows the basic schematic of DAB converter.

A non-resonant DAB topology has normalized load power and normalized voltage gain, all of which are related to phase shift ratio. The normalized load power and the normalized voltage gain are, however, determined by the normalized frequency in a resonant topology such as CLLC topology and LLC topology. In any case, things will become a lot easier if the frequency at which the resonant converter operates is the resonant frequency.

[15] derivated a comprehensive analysis for an isolated bidirectional DC/DC converter (IBDC) for the solid-state transformer (SST) application. The comparison is carried out between full-bridge CLLC converter, half-bridge CLLC converter, full-bridge DAB converter and half-bridge DAB converter. The result shows that the half-bridge CLLC is the most suitable choice for the 1kW application with the advantages of high power density and low cost. [16] also has the same selection for the half-bridge CLLC, but the results indicate high current stress in the converter. As a result, the half-bridge topology will not be considered in this project due to the bidirectional power flow.

Comparing the CLLC and DAB, many papers such as [12] [13] [9] and [15] shows the results that CLLC could achieve ZVS in the whole load range whereas DAB will lose ZVS at light load but the ZVS range could be extended with complex modulation techniques such as double phase control and triple phase control. Another advantage of CLLC is that the resonant capacitors keep the flux balanced and maintain the high resonant frequency with the resonant inductors [11]. As a result of the symmetrical resonant tank design in the CLLC converter, the power conversion operation and efficiency on both sides are the same. As for the loss aspect, CLLC holds higher conduction loss due to the larger RMS current, but it holds ZVS turn-on over all load range and has lower switching turn-off loss [12]. And DAB might have higher switching loss with the possibility of losing ZVS at light load. The comparison result is summarized in Table 2.1. [17]

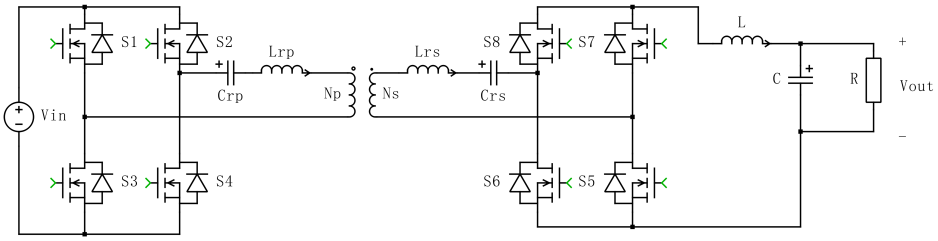

Figure 2.5: CLLC Resonant Converter Schematic

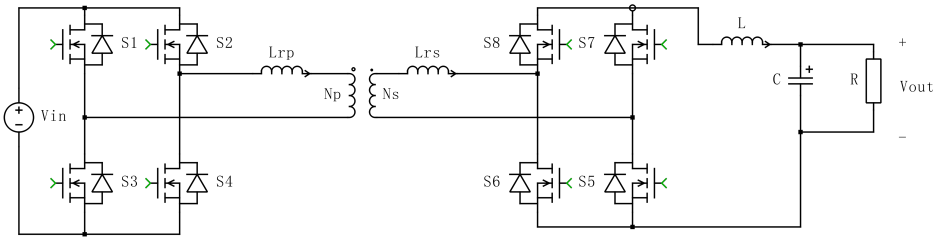

Figure 2.6: DAB Converter Schematic

Comparing the two identical single-output DC-DC converters and one dual-output converter, the dual-output converter has the advantage of saving 4 switches on the primary side which contributes to lower cost and higher efficiency. So the two dual-output converter topologies, Triple Active Bridge and Multiport CLLC will be presented in the following sections.

Table 2.1: Comparison between CLLC and DAB

	CLLC	DAB
ZVS	whole load range	lose ZVS at light load but with modulation techniques ZVS range is extended
Recommended Modulation	Frequency Control	(Triple) Phase Control for extended ZVS range
Advantage	resonant capacitors provide automatic flux balancing	less total loss and higher efficiency
Disadvantage	higher loss and RMS current complex resonant tank design	light load ZVS but need extra inductor high dv/dt
Conduction Loss	higher	lower

2.1.2. Dual Output DC-DC Converter

Multiple ports being integrated using different power converters is not feasible due to the cost and number of switches involved. Rather than creating many converters with their ports, a multiport converter (MPC) was proposed by [18]. As a result of the multiport converter, multiple power sources with their own input ports and output ports are connected through a single power converter to transfer power between them. As a result, redundant stages of power conversion and unnecessary semiconductor switches are removed from the primary side of isolated converter topologies. It is important to have such a converter available for the use of electric vehicles in order to control various sources of energy as well as stabilize the DC grid for the use of EVs.

Triple Active Bridge Converter

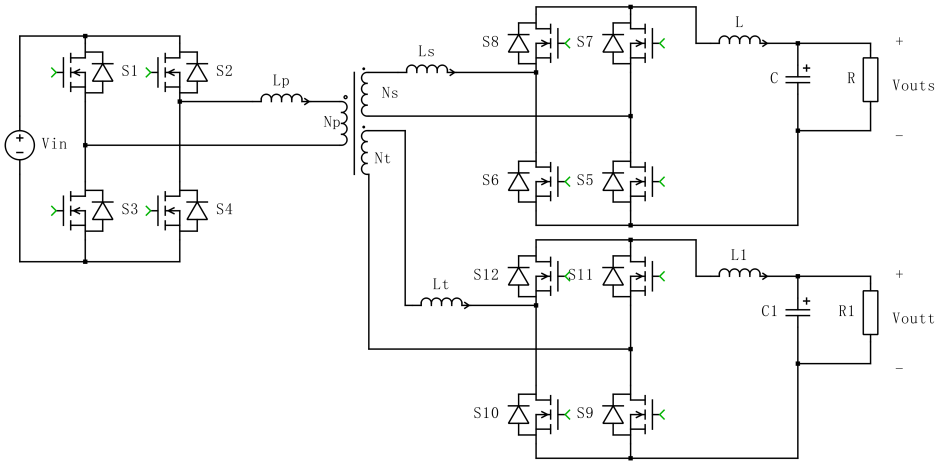

Figure 2.7: Triple Active Bridge Schematic

The Triple Active Bridge (TAB) converter, classified as a multiport converter (MPC), features three full bridges interconnected by a multiwinding high-frequency (HF) transformer derived from the Dual Active Bridge (DAB) topology. But there's a huge gap between DAB and TAB, there are three more parameters brought by the additional port in the transformer current expressions, including the port voltage, duty cycle and phase shift angle of the third port Serving as a versatile energy management system, the TAB converter enables seamless integration and bidirectional energy transfer among multiple ports while ensuring complete electrical isolation between them. This capability proves advantageous in accommodating varying port voltage levels and facilitates efficient energy exchange. The fundamental modulation scheme employed in the TAB converter entails utilizing 50% duty cycles across all full bridges while exploiting the phase shifts between the three leakage inductors to facilitate power transfer between the different ports. This modulation strategy facilitates optimal power flow control and regulation within the multiport system, thereby enhancing its overall performance and functionality [19].

However, the phase shift between the ports provides two degrees of freedom, both of which have the chance of loss of soft-switching and high circulating current. To improve that, the parasitic capacitance was considered to derive zero voltage switching boundaries in [19]. This study provides an in-depth derivation of the Zero Voltage Switching (ZVS) range in the context of the Triple Active Bridge (TAB) converter. The analysis takes into account the influence of parasitic capacitance, which introduces a soft-switching condition. This condition manifests as a low current in the leakage inductance that is necessary to facilitate ZVS commutation. By considering the impact of parasitic capacitance, a comprehensive understanding of the ZVS behaviour in the TAB converter is achieved, enabling the optimization of operating conditions and improved overall performance. As a result, the port with higher voltage in TAB could achieve ZVS easier than the other two ports and the phase shift inside the full bridge could be implemented for that port in order to expand the ZVS region of the ports with lower voltages.

Decoupling Control Methods

The design and control of the TAB converter pose a significant challenge due to the inherent cross-coupling of power flows between the ports resulting from the presence of a multi-winding transformer. This characteristic renders the TAB converter akin to a multi-input multi-output (MIMO) system with interdependent control loops. Consequently, addressing the interplay and coordination of these coupled control loops becomes essential for achieving efficient and reliable operation of the TAB converter. And all the decoupling control methods have one main goal which is to simplify the cross-coupled MIMO control loops into several independent SISO control loops.

A power flows decoupling controller for TAB is proposed in [20]. The controller is based on a full-order continuous-time model of TAB derived using the GAM (generalized average modelling) technique

which uses the Fourier series expansion to divide state-space variables into active and reactive power components. Between the three ports of the converter, active power flows are decoupled by the transformer currents.

In order to precisely forecast the instantaneous current and voltage waveforms, a novel modelling approach called generalised-harmonic-approximation (GHA) is introduced in the work by [21]. This modelling method is complemented by an efficient control strategy that facilitates high conversion efficiency and Zero Voltage Switching (ZVS) operation. When compared to conventional phase-shift modulation techniques, the proposed method exhibits the advantage of extending the operational range of simultaneous charging operation mode. By leveraging this innovative approach, accurate waveform prediction, optimal power flow control, and expanded operational capabilities can be achieved, resulting in improved converter performance and efficiency.

A state feedback controller and a decoupled controller are designed and modelled in [22] for the decoupled control of TAB. A new decoupling matrix-based proportional-integral (PI) converter design method is proposed for the decoupled controller to reduce the design complexity and improve the system's dynamic performance. And the performance is compared with the state feedback controller to prove the improved performance such as lower settling time and lower overshoot or undershoot. The research by Chandwani et al. [23] introduces a novel decoupled controller that employs cross-gain compensation to effectively counteract the impact of cross-coupling terms. The study discusses two distinct approaches to achieve decoupled control, as outlined in [23]. The first approach involves modifying the plant to eliminate the influence of cross-coupling terms, which is designed in [24] and will be introduced in the following. The second approach, which is specifically selected in [23], incorporates a counter-reactive cross-gain term within the control block to minimize the effect of cross-coupling. By implementing this chosen approach, the proposed decoupled controller successfully addresses the undesired interaction between control loops, resulting in improved system performance and stability.

In the study by Bandyopadhyay et al. [24], a modified configuration of the Multiactive Bridge (MAB) converter is proposed. This modified configuration incorporates a voltage source connected to the magnetizing inductance of the transformer. The unique feature of this configuration is its ability to provide inherently decoupled power flows and independent power flow control tuning for the multiple ports. The underlying concept involves adjusting the leakage inductance of one port to be relatively small when viewed from the other ports. This design approach effectively regulates the voltage across the magnetizing impedance of the transformer, resulting in decoupled power flow between the remaining two ports. This innovation enables greater flexibility in power flow control and enhances the overall performance of the multiport converter system. But external inductors are required for the other ports in order to have the decoupled configuration.

Multiport CLLC Resonant Converter

Fig.2.8 shows the basic schematic of the multiport CLLC resonant converter. A multiport CLLC convert with three half-bridges was proposed in [25], each port can be a load or a source and the converter behaviour is as expected for DC transformers. And there is no need to use active control in the system with a fixed switching frequency near the resonant frequency in order to maximise the efficiency.

Another multiport isolated DC-DC converter for DC applications is proposed in [26] with full bidirectional power flow and simple control. Two bidirectional buck-boost stages are added to two of the three ports to provide controllable power exchange. The extra stages are served to control active power flow and the galvanic isolation is provided by the inner resonant stage of the resonant tank, which operates in open-loop control and changes its operation mode based on the actual power flow. [27] also shows a multiport converter for the reversible solid oxide fuel cell applications, where a multiport CLLC resonant converter is connected with an interleaved buck converter.

A novel bidirectional multiple port DC/DC transformer topology is presented in [28], the idea is based on the series resonant converter but with an extension of multiple output ports. The paper aims at integrating different converter stages and focuses on the power node with multiple ports in order to overcome the limitations of single power nodes. The key benefit is that there is only one magnetic component in the design, the transformer, and the leakage inductances form the resonant inductance. Unlike the control of the gate signals in the previous two papers, the full bridges in the three ports are synchronised switched with a 50% duty cycle. But the results are relatively the same. According to the experimental results, the LLC converter's inherent cross and load regulation leads to relatively small

voltage variations across the entire power range due to its cross- and load regulation. In this way, the converter can operate in an open loop at a fixed switching frequency and 50%duty cycle.

Another utilization of a three-port converter (TPC) is implemented in [14], which functions as a DC transformer with an LLC resonant tank for interfacing PV arrays with independent MMPTs, energy storage systems, and grid-connected inverters. Three operation modes are distinguished as single-input single-output (SISO), single-input dual-output (SIDO) and dual-input single-output (DISO). Based on the experimental results, the ZVS at the input port and ZCS at the output port can be easily obtained for the entire power range.

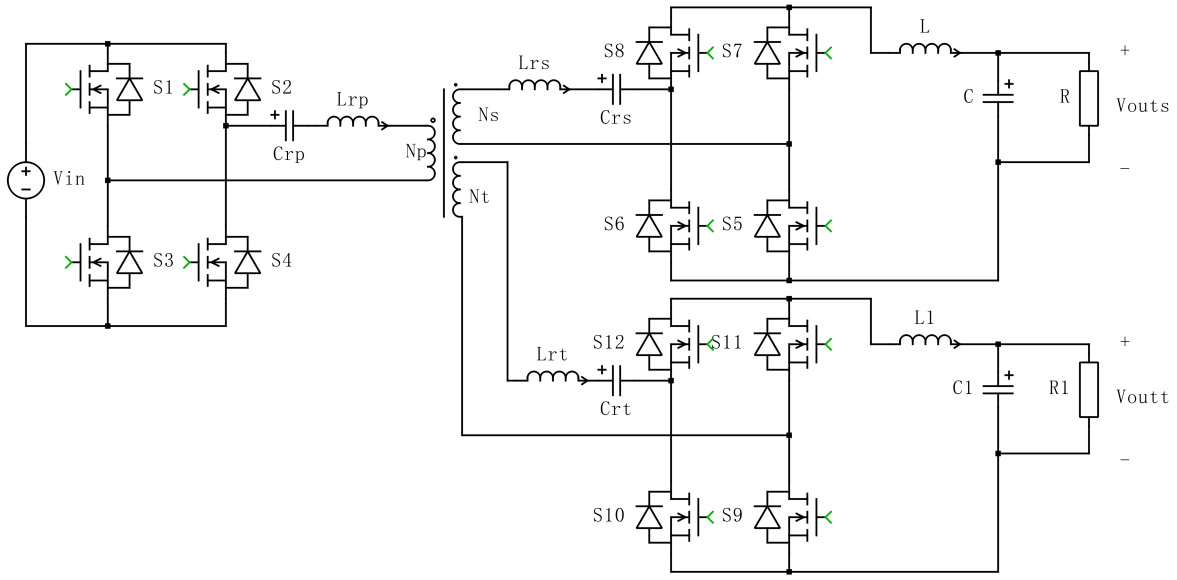

Figure 2.8: Multiport CLLC Resonant Converter Schematic

2.2. Interleaved Buck Converter

As previously discussed, the electric vehicle (EV) market is experiencing notable advancements, with EV manufacturers striving to improve the performance of power converters while simultaneously minimizing costs. In this context, the DC-DC buck converter serves as the final stage before connecting to the battery, playing a critical role in maintaining output current and current ripple within the battery's limits [29]. This ensures the efficient and reliable operation of the EV's power system while safeguarding the battery from excessive stress or damage.

Single-phase DC-DC converters are limited to applications with high currents due to the high loss caused by the i^2R loss in the inductor and the high ripple current in the inductor[30]. Interleaving, also known as multiphasing, is a useful technique to reduce the size of the filter component. By connecting half-bridges in parallel, the converter has inherently interleaving behaviour. It would then eliminate harmonics, increase efficiency, and have better thermal performance with high power density[31]. However, having interleaved will bring extra cost on additional inductors and active switches. The benefits of interleaving far outweigh the disadvantages it brings because the converter could deliver the desired output power with reduced size inductors and the split power flow also reduces power losses and thermal stresses on semiconductors [32]. Fig 2.9 shows the basic schematic of the two-phase interleaved buck converter.

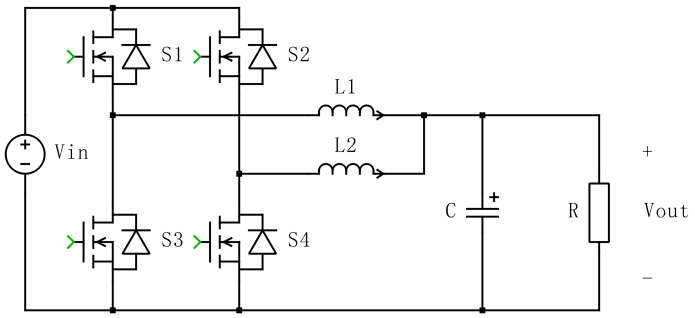

Figure 2.9: Two-phase Interleaved Buck Converter Schematic

2.2.1. Control Methods

Double Loop Control

Voltage mode control, peak current control, average current control, and sliding mode duty ratio control are some of the most common control techniques used on DC-DC converters. Current mode control offers a swift transient response when there is a demand for power at the upper level. When comparing peak current control and average current control, the latter holds the advantage of considering the converter's normal operating mode. By regulating the average current flowing through the inductor, average current control effectively governs the converter's output voltage. Conversely, peak current control is not well-suited for the discontinuous conduction mode (DCM) as it fails to accurately represent the average inductor current using the peak current alone. Consequently, employing a dual loop average current control, also known as cascade loop control, proves to be a better solution for the interleaved buck converter. In the following literature review, various applications of this double-loop control approach will be explored.

A thorough analysis and modelling of the interleaved buck-boost converter with a single PID controller are discussed in [31]. A new closed-loop control is simulated and achieves a higher efficiency compared with the conventional control performance. The PID controller acts as a compensation and the main purpose is to eliminate the error between the output voltage and the reference voltage. But the purposed control is heavily dependent on the load resistance, the efficiency is lower than 85% when the resistance is only 50 Ω. A voltage and current double closed-loop control strategy is applied in [33], but the inductor used in this paper is a coupling inductor. As a result, the inner loop of the current controller is split into two identical loops with half the reference current. Based on the observation in [33], due to the coupling inductor, the coupling coefficient has a great impact on the dynamic stability and ripple of the output.

Fig 2.10 shows a classic closed-loop system including a voltage loop regulator $PIv(s)$, current loop regulator $PIi(s)$ and the two output to duty cycle transfer functions $Gvd(s)$ and $Gid(s)$ [34, 35]. It is used as an easy method for connecting various photovoltaic modules with the purpose of improving power quality. The result shows that a properly tuned regulator can simplify and improve PV interleaving dynamically, steadily, and voltage-wise.

A different double-loop control strategy is shown in Fig. 2.11. The difference between Fig.2.11 and Fig. 2.10 is the transfer function of the plant in the outer voltage loop. In Fig. 2.11, the transfer function in the outer loop $Gvi(s)$ is the output voltage $V_o(s)$ to output current $I_o(s)$ but in Fig. 2.11, the transfer function in the outer loop is the output voltage $V_o(s)$ to duty cycle ratio $d(s)$.

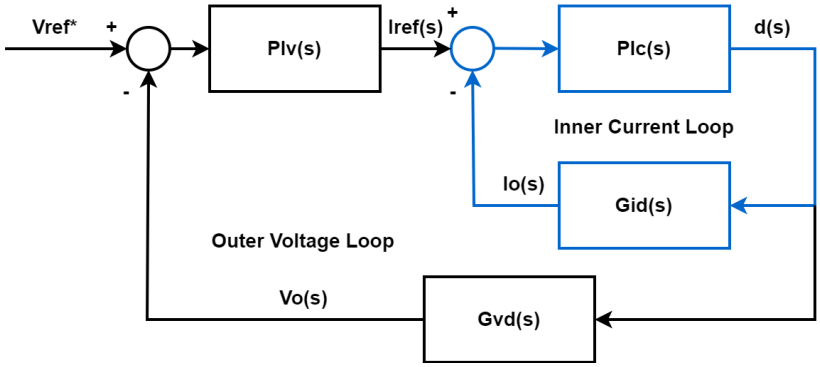

Figure 2.10: Cascade PI Control for Interleaved Buck Converter

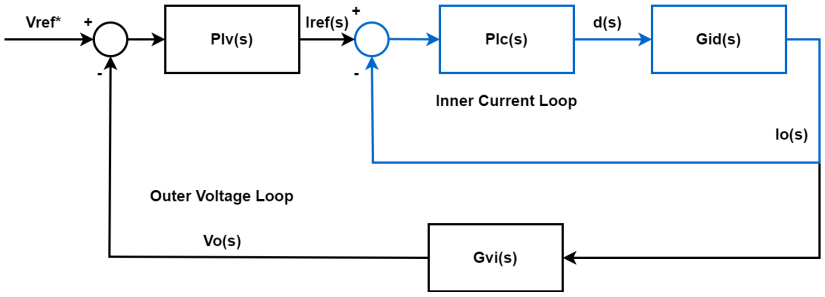

Figure 2.11: Double Loop Control for Interleaved Buck Converter

Sliding Mode

As introduced above, the linear compensators, e.g. PI controllers, have wide use in switch mode power stages controls. With parametric variations, system response will deteriorate as the dynamic performance of the converter is based on small-signal average models of converters. As shown in [36], when the operating point varies and the equivalent load impedance varies as well, the performance of the PV simulator that is controlled by PI controllers. Thus, to overcome the drawbacks and ensure robustness against the parameter variations, sliding mode controllers (SMC) were proposed and put into practice. In [36], a novel sliding mode duty-cycle controller (SMDC) is used as a regulator of a three-phase interleaved buck converter that is part of the solar simulator's power stage, thus providing high control bandwidth while providing a highly efficient model of the PV system. But synchronised current sensing is necessary when using dc-link current sensors to determine phase currents.

Unlike the conventional SMDC that uses hysteresis modulation which output is directly used as gate signals. The paper by Tan et al. [37] provides a comprehensive design procedure for the SMDC (Single-Mode Duty Cycle), which introduces a pulse width modulation (PWM) based sliding mode voltage controller as an alternative to hysteresis modulation. The design approach involves the indirect translation of the SM control law. Initially, the formulation of the equivalent control signal, a continuous function derived from the discrete input function, is achieved through the establishment of invariance conditions. Subsequently, the equivalent control function is integrated into the immediate duty cycle function of the PWM modulator, enabling seamless integration into the SMDC framework. An improved SMDC is proposed in [38] for a DC-DC buck converter with constant power loads. The output of the SMDC is the duty ratio, which serves as the basis for generating PWM gate signals for the converter. This enhancement empowers the converter to effectively stabilize DC power systems across the entire operating range, even in the face of substantial fluctuations in load power and supply voltage.

3

System Design and Comparison

3.1. System Design Overview

After the literature review was carried out, it could be concluded that the use of a multiport converter (MPC) has the advantage of reducing the switching devices on the primary side with a lower cost and higher efficiency as a result of the reduction in switching devices. Hence, two typical MPCs (Multiport CLLC converter and Triple Active Bridge converter) will be modelled and simulated for the purpose of selecting a suitable topology. In the following sections, simulation results will be presented and their performances compared for the topology selection of the EV charger.

The following are the details of two charging operational modes that will be discussed. In order to demonstrate the bidirectional power flow of both topologies, the discharging mode will also be simulated.

- Single Input Single Output (SISO): one car is charged with a maximum power of 11 kW by the grid and the other output port is disconnected.
- Single Input Dual Output (SIDO): two cars are charged simultaneously with an equal output power of 5.5 kW by the grid.

3.2. Triple Active Bridge

3.2.1. Working Principle

Generally speaking, the smaller the inductance of the AC link, the greater the converter's ability to transfer power. The AC link inductance is directly influenced by the leakage inductance of the high-frequency transformer. When the leakage inductance is minimal, an additional inductor is required to shape the current and enable Zero Voltage Switching (ZVS) for improved efficiency [39]. The transferred power could be calculated as Eq.3.1, where the maximum power is transferred when $\phi = \frac{\pi}{2}$.

$$P_{12} = \frac{nV_1V_2}{2\pi f_s L}\phi(1 - \frac{|\phi|}{\pi}) \tag{3.1}$$

As an extension of the Dual Active Bridge (DAB), the Triple Active Bridge (TAB) is an enhanced version of the Dual Active Bridge (DAB). In this case, there is an additional full bridge as a third port and another winding is added to the HF transformer which is coupled with the other windings. An equivalent delta circuit of TAB is shown in Fig.3.2. Each port of TAB is connected to the others through an inductance. The amount of power transferred by each port could be determined by the inductance value and the phase shift between these ports, similar to DAB power transfer Eq.3.1.

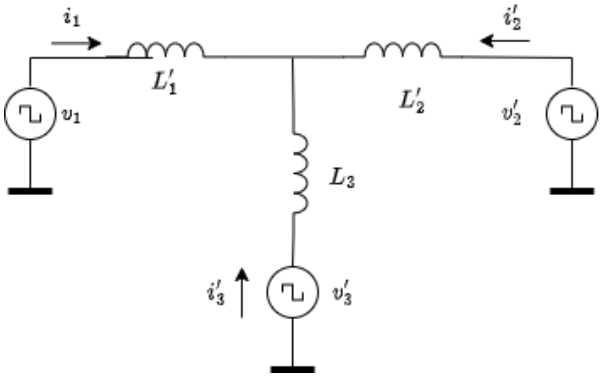

Figure 3.1: TAB Converter Star Equivalent Circuit

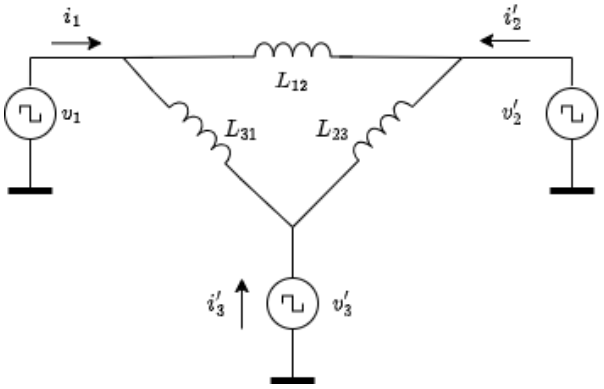

Figure 3.2: TAB Converter Delta Equivalent circuit

The inductance L_{12}, L_{13} and L_{23} could be calculated as

$$\begin{aligned} L_{12} &= \frac{L_{l1}L'_{l2} + L_{l1}L'_{l3} + L'_{l2}L'_{l3}}{L'_{l3}} \\ L_{13} &= \frac{L_{l1}L'_{l2} + L_{l1}L'_{l3} + L'_{l2}L'_{l3}}{L'_{l2}} \\ L_{23} &= \frac{L_{l1}L'_{l2} + L_{l1}L'_{l3} + L'_{l2}L'_{l3}}{L_{l1}} \end{aligned} \tag{3.2}$$

where L_{l1}, L_{l2} and L_{l3} are the leakage inductance of each port of the transformer in its star equivalent circuit referred to port 1, as shown in Fig.3.1 and they could be calculated by using the self and mutual inductances of the transformer as :

$$\begin{aligned} L_{l1} &= L_{11} - \left(\frac{N_1}{N_2}\right) L_{12} \\ L_{l2} &= L_{22} - \left(\frac{N_2}{N_1}\right) L_{21} \\ L_{l3} &= L_{33} - \left(\frac{N_3}{N_1}\right) L_{13} \end{aligned} \tag{3.3}$$

The phase shifts ϕ_2 and ϕ_3 have to be selected properly in order to achieve required power values[40]. The maximum phase shift with maximum power output could decide the value of the leakage inductance of the TAB. And then the corresponding phase shift with different power ratings could be calculated using the formulas below.

$$
\begin{aligned}
P_1 &= \frac{\phi_2\left(\pi-\phi_2\right)V_1V_2L_3+\phi_3\left(\pi-\phi_3\right)V_1V_3L_2}{2\pi^2 f_s\left(L_1L_2+L_2L_3+L_3L_1\right)} \\
P_2 &= \frac{\phi_2\left(\phi_2-\pi\right)V_1V_2L_3+\left(\phi_2-\phi_3\right)\left(\phi_2-\phi_3-\pi\right)V_2V_3L_1}{2\pi^2 f_s\left(L_1L_2+L_2L_3+L_3L_1\right)} \\
P_3 &= \frac{\phi_3\left(\phi_3-\pi\right)V_1V_3L_2+\left(\phi_2-\phi_3\right)\left(\pi-\phi_2+\phi_3\right)V_2V_3L_1}{2\pi^2 f_s\left(L_1L_2+L_2L_3+L_3L_1\right)}.
\end{aligned}
\tag{3.4}
$$

3.2.2. DC-Blocking Capacitors

As the name states, the DC-blocking capacitors are an effective method to maintain ZVS over a wide input voltage range and prevent magnetic saturation of the transformer, compared with other existing solutions such as peak current control [41] and ”magnetic ear” [42]. The peak current control has the chance of easily distorted sampling at high switching frequency and the magnetic ear requires an auxiliary core and an extra circuit to prevent transformer core saturation. As a result, including DC-blocking capacitance in the circuit is an easier method.

For the Dual-Active Bridge converter, it could achieve a wide efficiency range when the input and output voltage has unity gain. If the voltage ratio changes, the efficiency of DAB will decrease significantly. Thus a new modulation scheme has been proposed in [43], by introducing a voltage offset across the DC-blocking capacitor connected in series with the transformer. When the output voltage is twice its input voltage, by regulating only the phase angle between the two ports, a wide ZVS range could still be obtained. The DC-blocking capacitance is put at the primary side of the transformer whenever the reflected input voltage is much higher than the output voltage so that it could maintain soft-switching when the output voltage rises close to twice the input voltage.

A different hybrid modulation for using a DC-blocking capacitor in DAB is proposed in [44]. This method is designed for a 0.5-voltage ratio between the output voltage and input voltage. By turning the primary bridge into a voltage halver, the soft switching range is extended and the efficiency is improved. By choosing different modulation modes, a full ZVS range could be obtained, and detailed modulation is concluded in Table3.1. The DAB schematic is shown in Fig.2.6, referring to the corresponding switches for the half-bridge modulation.

Table 3.1: Hybrid Modulation Modes for DC-Blocking Capacitors and SPS Comparison

Parameter	Conventional SPS	HB/FB	FB/HB	HB/HB
nV_o/V_{in}	=1	<1	>1	(improve DAB converter at light load)
voltage ratio	1	0.5	2	1
Switches	50% duty cycle	S4 ON S2 OFF	S5 ON S8 OFF	S4&S5 ON S3&S8 OFF

3.2.3. Simulation Results

There are two conditions that are taken into consideration for the charging progress. The first is to charge two cars at the same time, each port has an output power of 5.5kW. Another condition is charging one car with a maximum power of 11kW.

SIDO at 5.5kW

For Triple Active Bridge, in order to charge two cars at the same time, the phase shift between the primary and the secondary and the phase shift between the primary and the tertiary will be the same which is $\frac{\pi}{4}$. The result is shown in Fig.3.3, the first two plots at the top show the primary and secondary gate signals, also showing the phase shift between the two sides. The two plots at the bottom show the input current of the transformer and the two identical output currents of the transformer. It could be seen from the figure that there is also a phase difference between the primary current and the secondary and tertiary current. Fig.3.4 shows that the two output ports all reach 5.5kW with the properly designed

phase shifts. The properly designed phase shifts could be calculated using the following equations, where $V_i(i = 1, 2, 3)$ are the voltages across the input and output voltages and $L_i(i = 1, 2, 3)$ are the three inductors. P_1 is the input power and P_2 and P_3 are the two output powers. Under the SIDO condition, $P_1 = 11kW$ and $P_2 = P_3 = 5.5kW$.

$$
\begin{aligned}
P_1 &= \frac{\phi_2(\pi - \phi_2)V_1V_2L_3 + \phi_3(\pi - \phi_3)V_1V_3L_2}{2\pi^2 f_s(L_1L_2 + L_2L_3 + L_3L_1)} \\
P_2 &= \frac{\phi_2(\pi - \phi_2)V_1V_2L_3 + (\phi_2 - \phi_3)(\phi_2 - \pi - \phi_3)V_21V_3L_1}{2\pi^2 f_s(L_1L_2 + L_2L_3 + L_3L_1)} \\
P_3 &= \frac{\phi_32(\pi - \phi_3)V_1V_2L_3 + (\phi_2 - \phi_3)(\phi_2 - \pi - \phi_3)V_2V_3L_1}{2\pi^2 f_s(L_1L_2 + L_2L_3 + L_3L_1)}
\end{aligned}
\tag{3.5}
$$

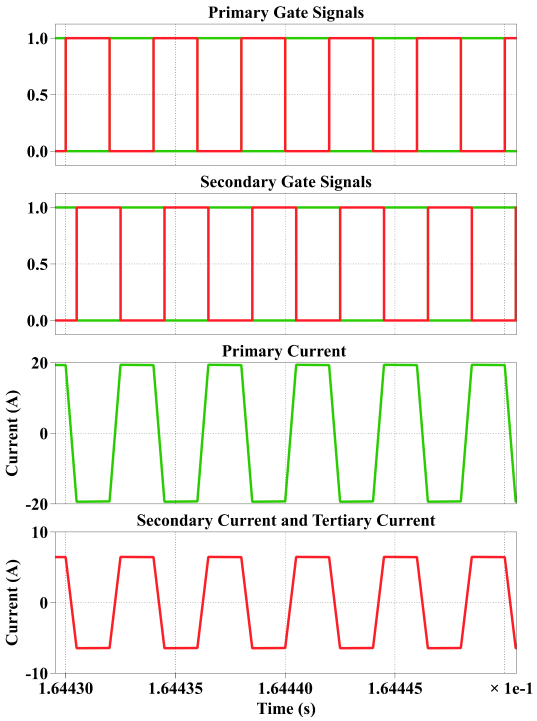

Figure 3.3: TAB Current with Gate Signals when $P_{out} = 5kW$

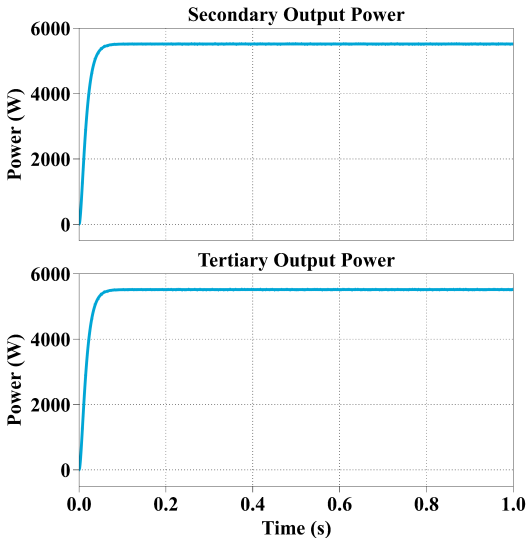

Figure 3.4: TAB Secondary and Tertiary Output Power at 5.5KW

Figure 3.5: TAB Output Performances at $P_{out} = 5kW$

SISO at 11kW

To charge one car at full power, the phase shift between the primary and secondary and the phase shift between the primary and tertiary are modified in order to obtain the condition that the secondary port has the maximum 11kW output power and the tertiary port has almost zero power. The phase difference between the primary and secondary sides is designed at the maximum phase shift $\frac{\pi}{2}$ in order to maintain the maximum power of 11kW. The tertiary phase shift is calculated based on Eq.3.5. Under the SISO condition, $P_1 = 11kW$ and $P_2 = 11kW$ and $P_3 = 0kW$.

The result is shown in Fig.3.6, the first two plots at the top show the primary and secondary gate signals, also showing the phase shift between the two sides. The two plots at the bottom show the input current of the transformer and the two identical output currents of the transformer. It could be seen from the figure that there is also a phase difference between the primary current and the secondary and tertiary current. Fig.3.7 shows that the secondary port reaches 11kW maximum power output with the properly designed phase shifts. Meanwhile, the tertiary port has almost zero output power.

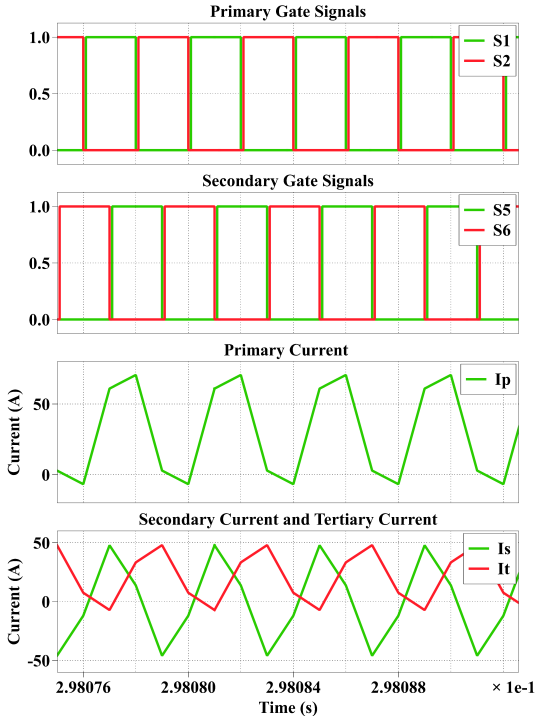

Figure 3.6: TAB Current with Gate Signals when $P_{out} = 11kW$

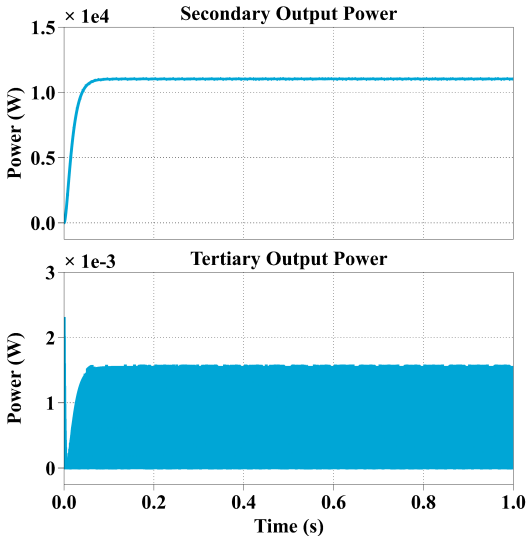

Figure 3.7: TAB Secondary and Tertiary Output Power at 11KW

Figure 3.8: TAB Output Performances at $P_{out} = 11kW$

3.3. Multiport CLLC Resonant Converter

3.3.1. Working Principle

Fig.3.9 shows the equivalent circuit of the multiport CLLC converter at SIDO operation mode. The transformer is a three-winding high-frequency transformer with the same turns ratio for the secondary and tertiary windings, equipped with three full bridges. In order to achieve high efficiency, the CLLC topology is used and operated in the open-loop mode slightly below the resonant frequency. Because of the full bi-directionality of the three ports, the structure of the resonant tank requires symmetry. As a result, the resonant tank is split between all three ports instead of being located on one single port. Each resonant tank contains of a resonant capacitor C_{r_i} and an leakage inductor L_{r_i}, where $i = p, s, t$.

The resonant part is designed to function like a DC transformer without requiring any complex controls. According to the direction of power flow, it can only be controlled by activating or deactivating PWM on the three full bridges. Only the power-supplying ports are actively switched, while the load ports are turned off, utilizing their free-wheeling diodes as passive rectifiers.

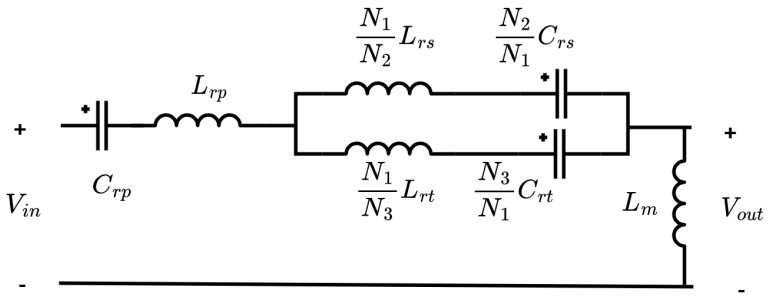

Figure 3.9: Multiport CLLC Resonant Converter Equivalent Circuit

3.3.2. Resonant Tank Design

The resonant tank is distributed among the three ports due to the bidirectional power flow, but it could be designed using the criteria from a single resonant tank design.

The resonant currents are estimated from the DC values using the first harmonic approximation (FHA).

$$\begin{aligned} V_{AC}(t) &= \frac{2}{\pi} V_{DC} \sin\left(2\pi f_{sw} t + \varphi_v\right) \\ I_{AC}(t) &= \pi I_{DC} \sin\left(2\pi f_{sw} t + \varphi_i\right) \end{aligned} \tag{3.6}$$

The effective DC loads are modelled as resistors and referred through a rectifier to equivalent AC loads:

$$\begin{aligned} R_{DC} &= \frac{V_{DC}^2}{P} \\ R_{AC} &= \frac{2}{\pi^2} R_{DC} \\ R_{AC_{\text{min}}} &= \frac{2V_{DC}^2}{\pi^2 P_{\text{max}}} \end{aligned} \tag{3.7}$$

The behaviour of a single resonant tank could be represented by the quality factor Q which is defined as the ratio of the tank impedance Z_r and the effective AC load R_{AC} calculated above.

$$\begin{aligned} Q_i &= \frac{Z_{r_i}}{R_{AC}} \\ Z_{r_i} &= \sqrt{\frac{L_{r_i}}{C_{r_i}}} \end{aligned} \tag{3.8}$$

Fig below shows the normalized DC transfer function of the resonant tank for a given Q, the preferred operating region with ZVS behaviour is in the inductive part of resonant tank characteristics.

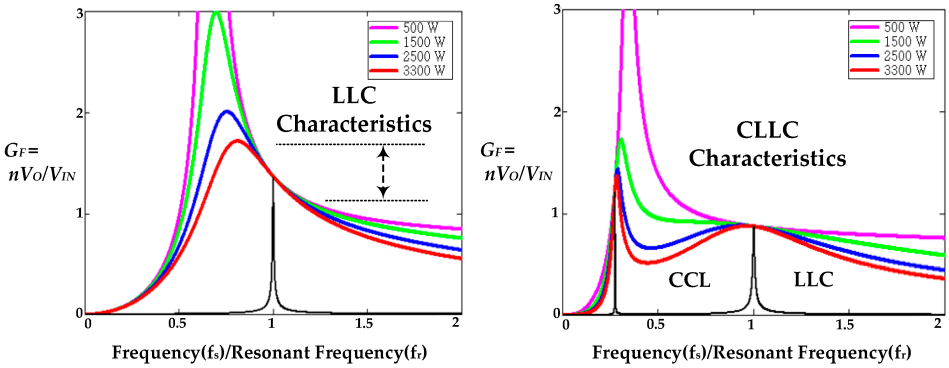

Figure 3.10: DC Gain of Multiport CLLC for no-load conditions [45]

$$f_r = \frac{1}{2\pi\sqrt{L_{eq} C_{eq}}} \tag{3.9}$$

In order to calculate the equivalent tank impedance, the sum of the sub-tanks and the parallel combination of the two remaining tanks could be taken into account, taking into account the transformer turns ratio [25].

$$L_{eq} = L_{rp} + \left(\frac{1}{\left(\frac{N_1}{N_2}\right)^2 L_{rs}} + \frac{1}{\left(\frac{N_1}{N_3}\right)^2 L_{rt}} \right)^{-1} \tag{3.10}$$

$$C_{eq} = \left(\frac{1}{C_{rp}} + \frac{1}{\left(\frac{N_2}{N_1}\right)^2 (C_{rs} + C_{rt})} \right)^{-1} \tag{3.11}$$

Each port should also work at the resonant frequency due to the synchronized switching. The common resonant frequency f_r is used to define the resonant capacitor of each sub-tank, so

$$\begin{aligned} f_r &= \frac{1}{2\pi\sqrt{L_{rp}C_{rp}}} \\ f_r &= \frac{1}{2\pi\sqrt{L_{rs}C_{rs}}} \\ f_r &= \frac{1}{2\pi\sqrt{L_{rt}C_{rt}}} \end{aligned} \tag{3.12}$$

The resonant capacitors and inductors of the multiport CLLC converter resonant tank are selected based on the performance and detailed values are listed in Table3.2. The resonance capacitance is selected as high as possible to decouple from the output capacitance ($50\mu F$) which is used to maintain an output voltage ripple of 3V.

Table 3.2: Multiport CLLC Resonant Converter Specifications

Inductor	Value	Capacitor	Value
L_{rp}	$50\mu H$	C_{rp}	$8.11nF$
L_{rs}	$6.6\mu H$	C_{rs}	$30.33nF$
L_{rt}	$6.6\mu H$	C_{rt}	$30.33nF$

3.3.3. Simulation Results

As discussed in the TAB section, there are two conditions that are taken into consideration for the charging progress. The first is to charge two cars at the same time, each port has an output power of 5.5kW. Another condition is charging one car with a maximum power of 11kW.

SIDO at 5.5kW

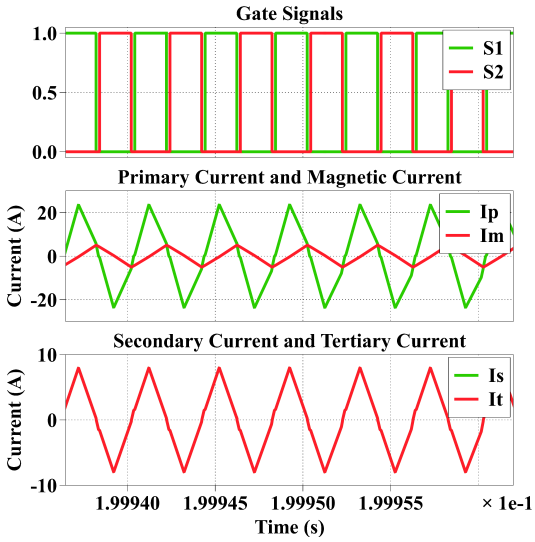

Figure 3.11: CLLC Current with Gate Signals when $P_{out} = 5kW$

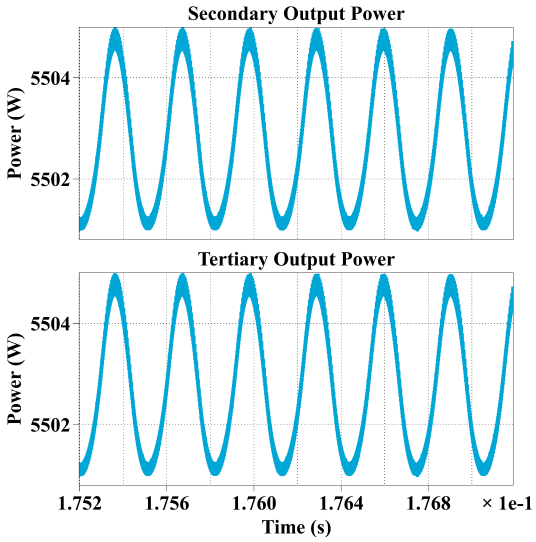

Figure 3.12: CLLC Secondary and Tertiary Output Power at 5.5KW

Figure 3.13: CLLC Output Performances at $P_{out} = 5kW$

For charging the two cars' condition, unlike TAB, as introduced above in the working principle part, the actively switched full bridge is the primary side bridge only. And the result is shown in Fig.3.11. The current of the primary side and the magnetizing current is presented in the second plot, showing that the resonant converter is operating at the resonant frequency. The secondary and tertiary current is shown in the last plot, the overlap waveforms indicating that the two output ports' currents are identical.

The output power result is shown in Fig.3.12. The two identical output power has a ripple of 4W and could reach 5.5kW which matches with the design of the converter.

SISO at 11kW

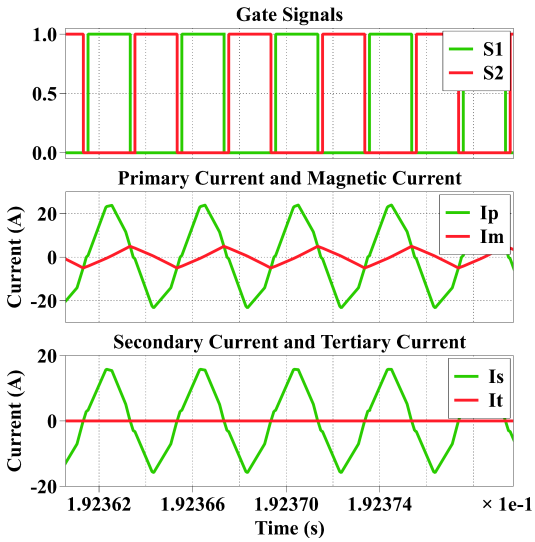

Figure 3.14: CLLC Current with Gate Signals when $P_{out} = 11kW$

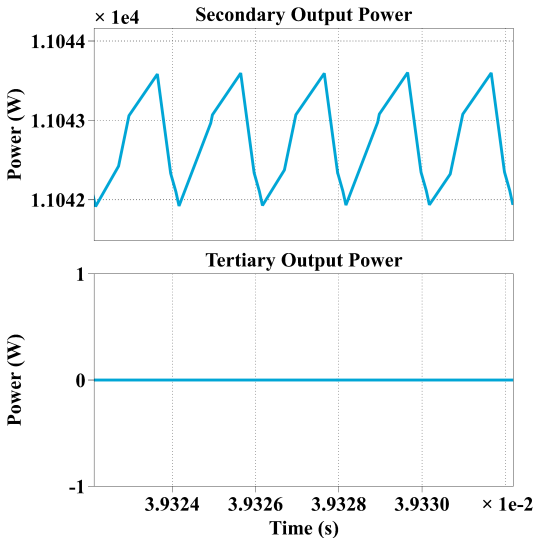

Figure 3.15: CLLC Secondary and Tertiary Output Power at 11KW

Figure 3.16: TAB Output Performances at $P_{out} = 11kW$

For charging one car at the maximum power condition, the results are shown in this section. Fig.3.14 shows the primary gate signals and the three ports' current with the magnetizing current of the transformer. The primary current and the magnetizing current show that the switching frequency is right at the resonant frequency. And the tertiary current is at zero due to the one output port condition. Because the only actively switched port is the primary port and the CLLC converter operates as an ideal DC transformer, if the tertiary port load is set to be infinite to simulate the open circuit, the full power will automatically flow to the secondary port which load is simulated as the 11kW load. And Fig.3.15 shows the output power of the secondary port is 11kW and the other output port power is zero.

3.4. Topology Performance Comparison

3.4.1. Capacitor Comparison

The number of capacitors is compared based on their effect on the transformer. A detailed comparison is shown in Table3.3 below, summarizing different modulation techniques and the outcomes. It could be seen from the table that the number of capacitance has little impact on the transformer voltage and current. The conclusion comes from Fig.3.18 and Fig.3.17. The figures on the right side in Fig.3.18 and Fig.3.17 are the zoomed region of the blue boxed area on the left side to have a clear view of the capacitance effect. It could be seen from Fig. 3.18 that with higher capacitance, the current is slightly higher in the circuit and the current and voltage are triangular waveforms because of the large step time. And it also could be seen from Fig. 3.17 that adding capacitance in a TAB converter will have some impact both on the voltage and current but the impacts are negligible compared with the high voltage and high current application.

Table 3.3: Number of Capacitor Comparison

Comparison Parameters	Without Capacitors	One Capacitor	Three Capacitors
Function/Topology	Triple Active Bridge	Used as DC-blocking capacitor to avoid DC magnetization of transformer	Dual-Output CLLC
Transformer Voltage	No significant change	No significant change	No significant change
Transformer Current	No significant change	No significant change	No significant change
Impedance Values	Larger characteristic impedance of the circuit because of low capacitance	Larger capacitance compared with resonant capacitance	Smaller capacitance compared with DC-Blocking capacitance
Capacitor Size	No capacitor	Smaller capacitor	Big capacitor in switching node under high voltage and high power

Consequently, the Triple Active Bridge with DC-blocking capacitors has little impact on the transformer, indicating there is no benefit in using such a large capacitor at the switching node in this high-

power and high-current EV charger.

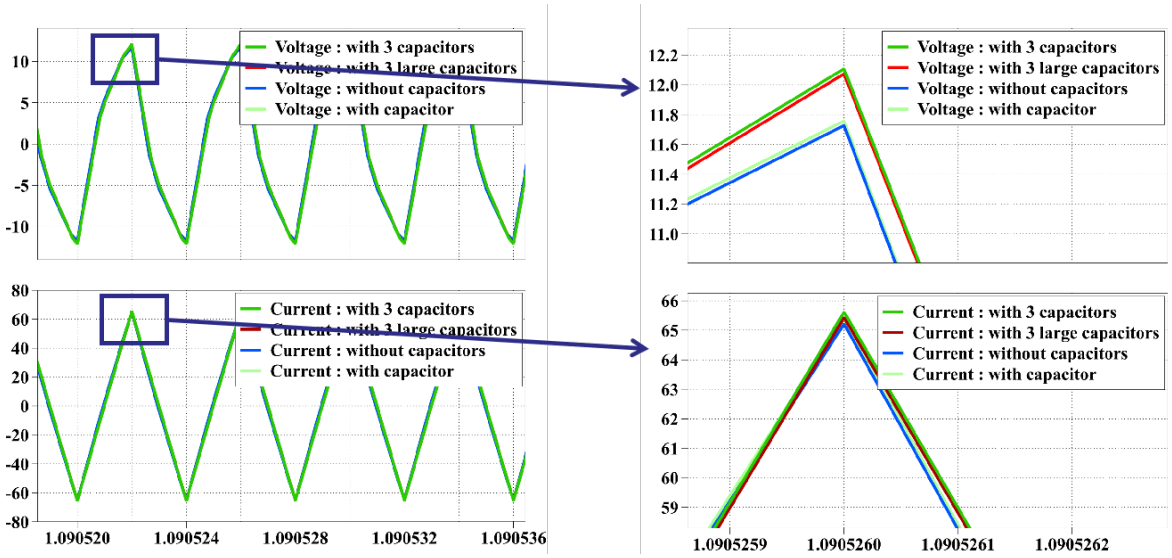

Figure 3.17: Capacitor Effect on the Transformer of CLLC

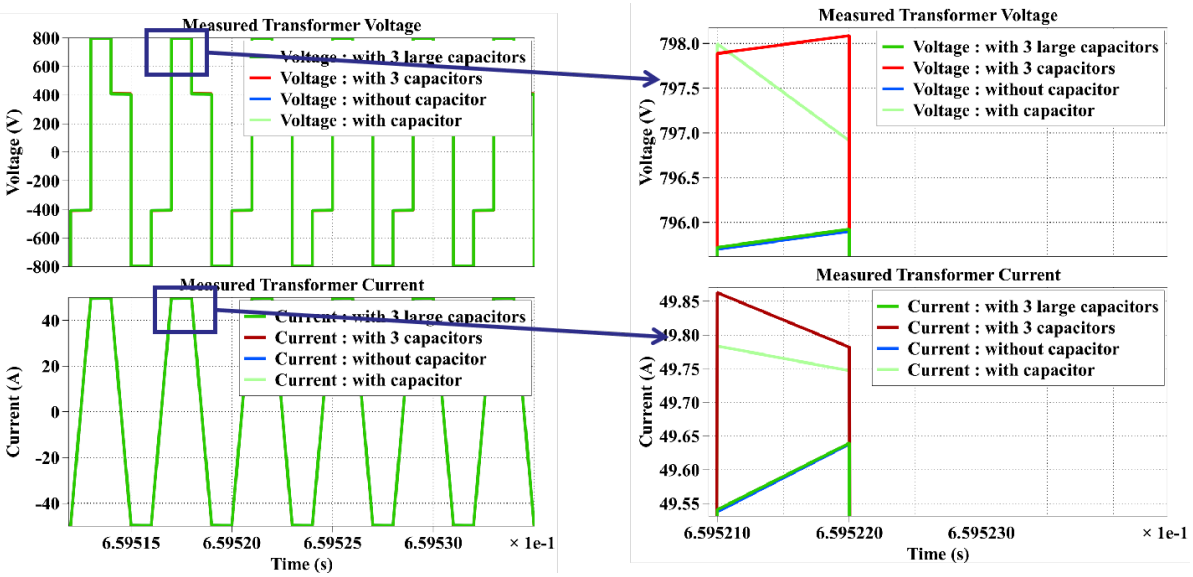

Figure 3.18: Capacitor Effect on the Transformer of TAB

3.4.2. Efficiency Comparison

The detailed simulation result for comparing the TAB and CLLC are listed below, Table3.4 shows the result under 5.5kW condition and Table3.5 shows the result under 11kW condition. It could be seen from both tables that when the switching loss of CLLC is lower than the switching loss of TAB. Also, the conduction loss of CLLC on the primary side is higher than the loss of TAB due to the higher RMS switch current in CLLC. In both power levels, the efficiency of CLLC is higher than TAB due to the low loss on the output side. Also, both topologies are considering soft switching, and zero turn-on loss in the simulation.

Table 3.4: TAB vs Multiport CLLC Based on System Specifications when $P_{out} = 5kW$

Comparison Parameter	TAB	Multiport CLLC
Output Voltage (V)	1066.03	1064.84
Output Power (W)	5500.35	5488.34
RMS Output Current (A)	5.16	5.154
Switching loss per switch (Primary) (W)	11.45	9.03
Switching loss per switch (Secondary) (W)	11.14	8.95
Conduction loss per switch (Primary) (W)	4.14	7.93
Conduction loss per switch (Secondary) (W)	0.83	0.69
Efficiency (%)	97.13	97.35

Table 3.5: TAB vs Multiport CLLC Based on System Specifications when $P_{out} = 11kW$

Comparison Parameter	TAB	Multiport CLLC
Output Voltage (V)	1064.79	1064.36
Output Power (W)	10977	10966.3
RMS output current (A)	10.30	10.30
Switching loss per switch (Primary) (W)	11.45	9.07
Switching loss per switch (Secondary) (W)	16.35	9.01
Conduction loss per switch (Primary) (W)	4.14	8.29
Conduction loss per switch (Secondary) (W)	8.56	2.93
Efficiency (%)	97.62	98.49

3.4.3. Thermal Performance

MOSFET Selection

Table 3.6: TAB MOSFET Selection

Product Number	Switching Loss (W)	Conduction Loss(W)	Total Loss (W)	RMS Current (A)
C3M0065100J	17.29	88.53	105.82	9.89696
C3M0120100J	40.76	188.84	229.6	9.82857
C3M0032120J1	12.93	8.42	21.35	9.89696
C3M0040120J1	15.50	20.50	36.00	9.82857

Due to the voltage specification of the dual output converter, the 1200V MOSFETs are selected for the output ports and the 1000V MOSFETs are compared for the input side. And the SiC MOSFETs need to be surface-mounted devices (SMD) for hardware design consideration. Table 3.6 and Table 3.7 show the loss comparison of different types of MOSFETs for TAB and CLLC. It could be seen from

both tables that $C3M032120J1$ has especially low values both in switching loss and conduction loss compared with other switches. So for the high-efficiency design purpose, the MOSFET with the lowest loss will be selected. $C3M032120J1$ is used for the twelve switches in both topologies, although for the primary side the voltage limit is a little bit high.

Table 3.7: CLLC MOSFET Selection

Product Number	Switching Loss (W)	Conduction Loss (W)	Total Loss (W)	RMS Current (A)
C3M0065100J	17.38	89.58	106.96	9.93273
C3M0120100J	40.90	191.49	232.39	9.87684
C3M0032120J1	13.00	8.51	21.51	9.93273
C3M0040120J1	15.62	20.81	36.43	9.87684

3.4.4. Result

Based on the comparison above, the advantages and disadvantages could be listed below.
For the triple active bridge converter:

- Advantages
  - A wide voltage gain and ZVS range
  - Lower conduction loss due to lower RMS switch current
- Disadvantages
  - Complex phase shift control to obtain the corresponding current level when the output port connection changes
  - Decoupling control or decoupling inductor configuration is needed

For multiport CLLC converter

- Advantages
  - No need for extra control loops, only constant frequency control is needed to maintain the switching frequency at the resonant frequency
  - High efficiency in both modes compared with TAB
- Disadvantages
  - Resonant frequency might not match with designed values in real-life transformer
    - but could be compensated by the extra pre-implemented resonant capacitors

To conclude, the main design objective is to design an effective, simpler and easier-controlled converter for the EV charger. Seen from the advantages and disadvantages above, the **multiport CLLC resonant converter** topology will be the most suitable solution for the EV charger among the compared topologies.

3.5. System Schematic Design

After selecting the multiport CLLC converter as the multiport converter topology, Fig.3.19 shows the illustration of the EV charger. At the bottom of the figure is the bipolar DC microgrids ranging from 600V to 800V, $\pm 350V$ is used as an illustration of the grid. Then the DC bipolar grid is connected to the primary side of the multiport converter which is selected as the multiport CLLC converter. Through the galvanic isolation provided by the transformer, the secondary and tertiary sides of the converter will provide an output voltage of around 1000V. Then the outputs of the multiport converter are connected with two identical interleaved buck converter which will handle the voltage regulation based on the connected EV batteries which might vary from 200V to 920V.

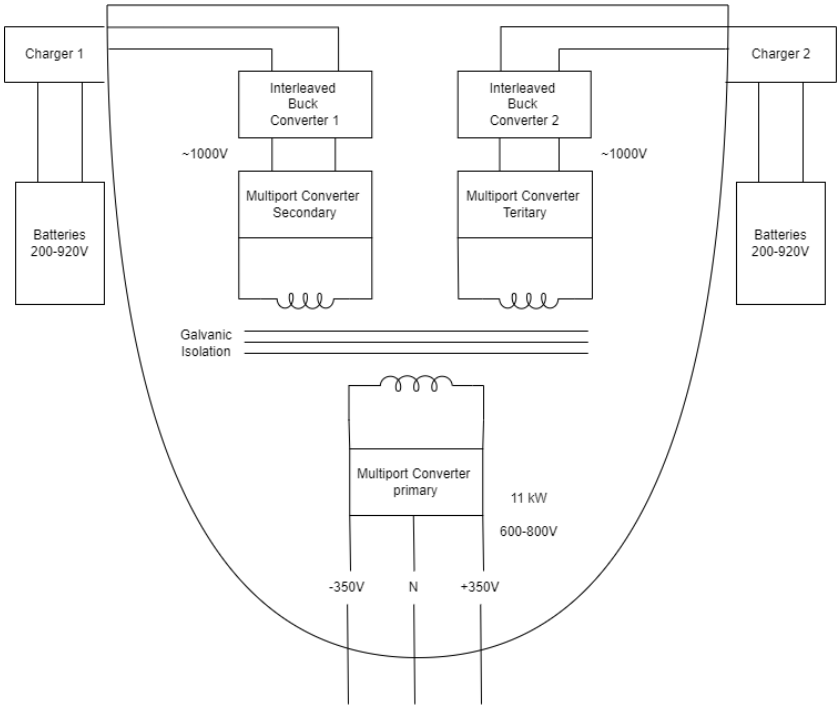

Figure 3.19: EV Charger Illustration

And the circuit schematic is shown in Fig.3.20. The yellow box circled is the Multiport CLLC resonant converter and the blue boxes circled are the two interleaved buck converters.The two interleaved 2-phase converters are connected at the two output ports of the CLLC converter.

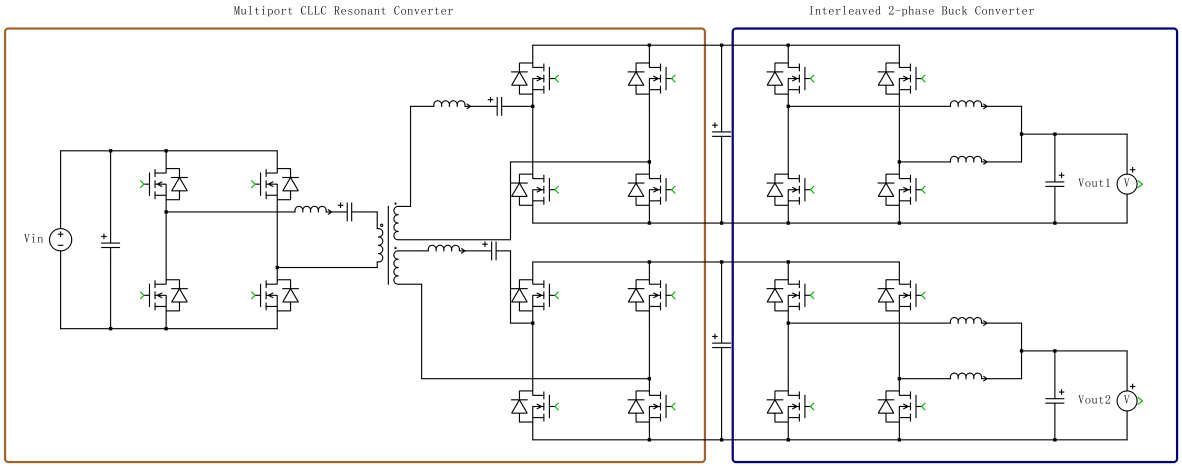

Figure 3.20: EV Charger Circuit Schematic

Fig.3.21 shows the simulation result of the whole EV charger converter without any control schemes. The result is just to show that both output ports could reach the maximum power of 11kW with the change of duty cycle. The simulation result with the control scheme will be presented in the next section after introducing the control logic of the converter.

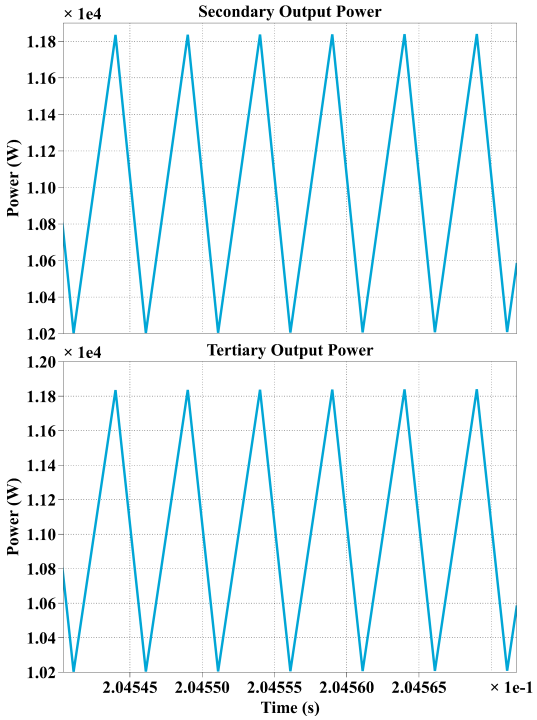

Figure 3.21: Output Power both at 11kW

4

Modelling and Control

In this chapter, the modelling of the interleaved buck converter will be presented with the performance comparison. And a suitable topology will be selected for the interleaved buck converter. Then the system level control will be introduced and discussed based on the theoretical design including the introduction of cascade PI control with saturation limit and the battery droop functions.

4.1. Interleaved Buck Converter Modeling and Comparison

4.1.1. Working Principle

As shown in Figure 2.9, S_1, S_2, S_3 and S_4 are four MOSFETs that are controlled in a complementary manner. Each of them is connected with an antiparallel diode for current flowing in both directions. The phase shift ϕ between different phases is determined by the number of phases in interleaved buck converter, as given by Eq. 4.1, where N is the number of phases. For a two-phase interleaved buck converter, $N = 2$, so the phase shift between the two half bridges is $180°$.

$$\phi = \frac{360°}{N} \tag{4.1}$$

As shown in Fig. 2.9, the inductors are non-coupled, so the inductor current ripple could be simply calculated as :

$$\Delta i_{L_1} = \frac{V_{out}}{L_1}(1 - D)T_s \tag{4.2}$$

$$\Delta i_{L_2} = \frac{V_{out}}{L_2}(1 - D)T_s \tag{4.3}$$

If $L_1 = L_2 = L$, then the inductor current ripple could be expressed as the equation shown below, where T_s is the switching period of the converter.

$$\Delta i_L = \frac{V_{out}}{L}(1 - D)T_s \tag{4.4}$$

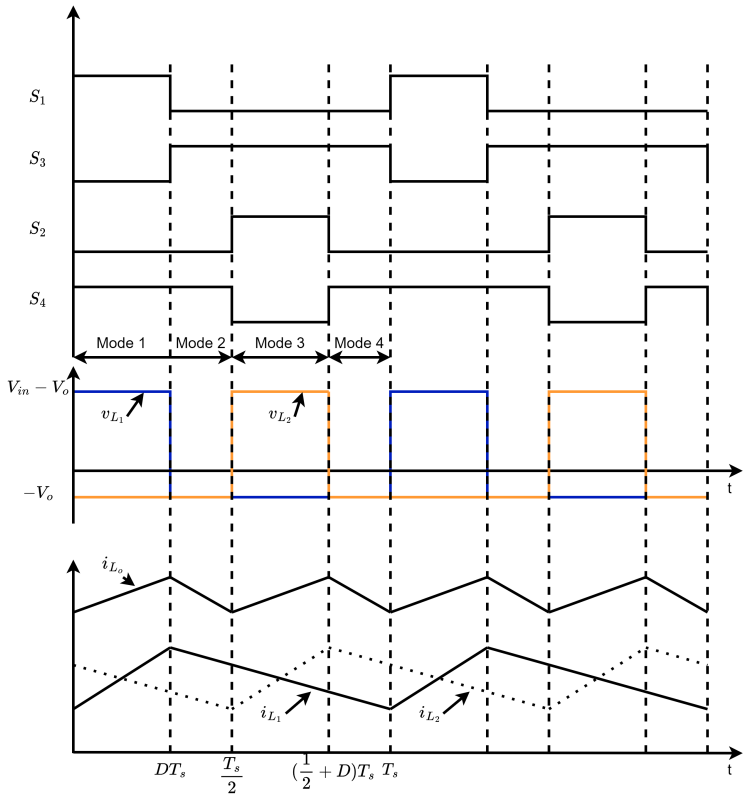

Figure 4.1: Interleaved Buck Converter Current Waveforms (D=0.5)

The output current is the sum of i_{L_1} and i_{L_2}, as shown in Fig. 4.1, the output current ripple occurs twice during one switching period, so the output current ripple is

$$\Delta i_{L_o} = \frac{V_{out}}{L}(1-2D)T_s \tag{4.5}$$

The duty cycle is expressed as

$$D = \frac{V_{out}}{V_{in}} \tag{4.6}$$

According to the design purpose of the converter, the duty cycle will range from 0.2 to 0.9 based on the EV battery voltage connected to the EV charger and the grid voltage.

Fig. 4.1 shows the current waveforms of inductors and output current when the duty cycle is smaller than 0.5. In mode 1, S_1 and S_4 are turned on and the other switches are turned off. The inductor L_1 is charged and L_2 is discharged. In mode 2, S_1 and S_2 are turned off and S_3 and S_4 are turned on, both inductors are discharged. In mode 3, S_2 and S_3 are turned on and the other switches are turned off, the inductor L_2 is charged and L_1 is discharged. In mode 4, S_1 and S_2 are turned off again, and the other two switches are turned on, thus the two inductors are discharged. Detailed inductor voltages and current directions in each mode are concluded in Table 4.1

Table 4.1: Operation Modes of Interleaved Buck Converter

	Mode 1	Mode 2	Mode 3	Mode 4
v_{L_1}	$V_{in} - V_o$	$-V_o$	$-V_o$	$-V_o$
v_{L_2}	$-V_o$	$-V_o$	$V_{in} - V_o$	$-V_o$
$\frac{d}{dt} i_{L_1}$	Positive	Negative	Negative	Negative
$\frac{d}{dt} i_{L_2}$	Negative	Negative	Positive	Negative
$\frac{d}{dt} i_{L_o}$	Positive	Negative	Positive	Negative

4.1.2. Simulation Result

In the case of the interleaved bidirectional converter, the mode of operation is influenced by the load characteristics [32]. If the converter operates in continuous conduction mode, it can experience conduction losses resulting from hard switching operations at high switching frequencies, as well as reversed diode recovery at low power levels. These factors contribute to efficiency challenges and potential power losses in the converter. However, considering the practical design and low current ripple, the inductor in the interleaved buck converter will be selected between $300\mu H$ and $400\mu H$.

Given the introduction of the working principles of interleaved buck converters in the previous subsection, this subsection aims to present a comparative analysis between buck converters with varying numbers of phases. Specifically, a standard buck converter, an interleaved two-phase buck converter, and an interleaved four-phase buck converter will be evaluated. The simulation results for these three converter configurations will be discussed to facilitate performance comparison and aid in selecting the most appropriate topology for the electric vehicle (EV) charger application. Furthermore, the consideration of inductor core size will be addressed, as employing two cores in parallel effectively doubles the core cross-sectional area, thereby reducing core loss and temperature.

Fig.4.2 shows the typical schematic of a conventional buck converter and Fig.4.3 shows the schematic of an interleaved four-phase buck converter. The inductors for the interleaved buck converter are selected as $400\mu H$ for a low inductor current ripple, according to Eq.4.5, compared with $300\mu H$.

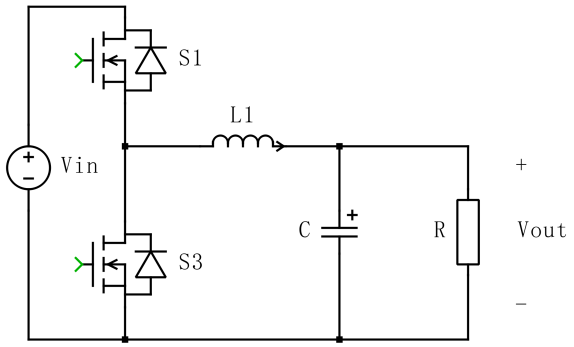

Figure 4.2: Conventional Buck Converter Schematic

The main purpose of the EV charger is to charge all kinds of batteries whose voltages vary from 200V to 920V. For the old version of batteries which range from 200V to 500V, the EV charger aims at charging it with the maximum current which is **20A**. For the new version of batteries with high battery voltages, the EV charger will charge it with maximum power which is **11kW**. So the duty cycle control of the interleaved buck converter is divided into two conditions when $D > 0.5$ the output current is determined by the output power and output voltage, and when $D < 0.5$ the output current is maintained at its maximum value (20A).

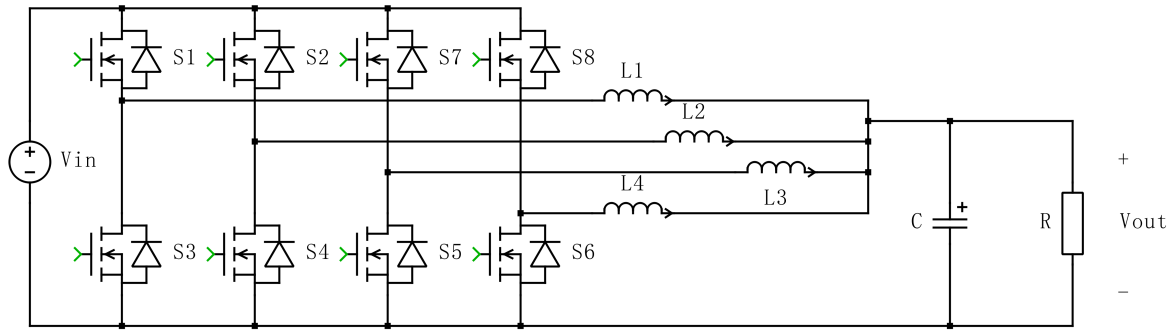

Figure 4.3: Four-phase Interleaved Buck Converter Schematic

The simulation results for the three topologies are shown below, the performances are compared mainly based on the inductor current and output current. As previously introduced, the converter will provide maximum current when the duty cycle is less than 0.5. Fig.4.4a shows the output current of the three converters, where the blue waveform represents the output current of the conventional buck converter, the red line represents the output current of the interleaved two-phase buck converter and the green line represents the output current of the interleaved four-phase buck converter. It shows that interleaving does have a great impact on reducing the output current ripple, comparing the blue line with the green and red lines. According to Eq.4.5 which is the output current ripple calculation of a two-phase interleaved buck converter, increasing the number of phases will reduce the output current as well but the difference is relatively small compared with the difference between the interleaved converter and the conventional converter.

Fig.4.4b shows the inductor current of the three topologies. As introduced before, the number of inductors in the circuits matches the number of phases in the converter. And the inductor current could be calculated as

$$I_L = \frac{I_o}{N} \tag{4.7}$$

where N is the number of phases. It could be seen from Fig.4.4b that the inductor current is reduced as the number of phases increases which means that the inductor losses and inductor temperature will also reduce. And because the inductances are all the same $(400\mu H)$ in the three circuits so the inductor current ripples are the same as shown in the figure. Numerical results and comparisons will be discussed in the following section.

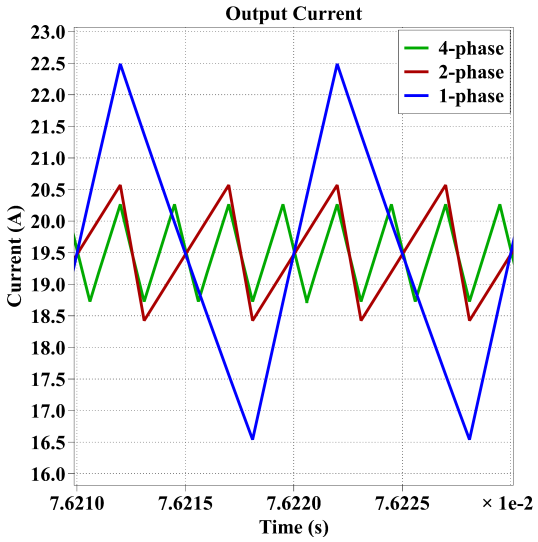

(a) Interleaved Buck Converter Output Current Result

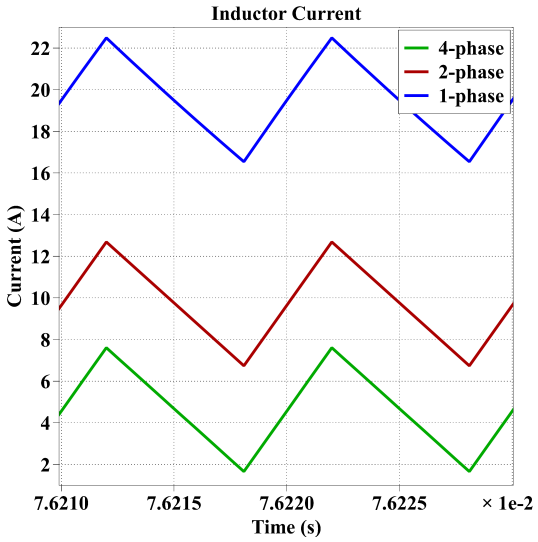

(b) Interleaved Buck Converter Inductor Current Result

Figure 4.4: Interleaved Buck Converter Simulation Result (D=0.4)

4.1.3. Result Comparison

Firstly, the worst-case consideration for the switch losses is simulated by changing the duty cycle ranging from 0.4 to 0.7. The result is shown in Fig4.5. It could be observed from Fig.4.5 that no matter how the number of phases varies, the total switch loss at $D = 0.5$ reaches the highest. The reason for $D = 0.5$ is the worst-case condition could be explained by the maximum average turn-on time of all the switches in the circuit.

The worst case at $D = 0.5$ also works for the inductor loss as shown in Fig.4.6. The inductor has the highest loss at $D = 0.5$ no matter how many phases are in the topology. And it also could be seen from the figure that as the increase in number of phases, the inductor loss decreases significantly due to the reduction of the inductor current.

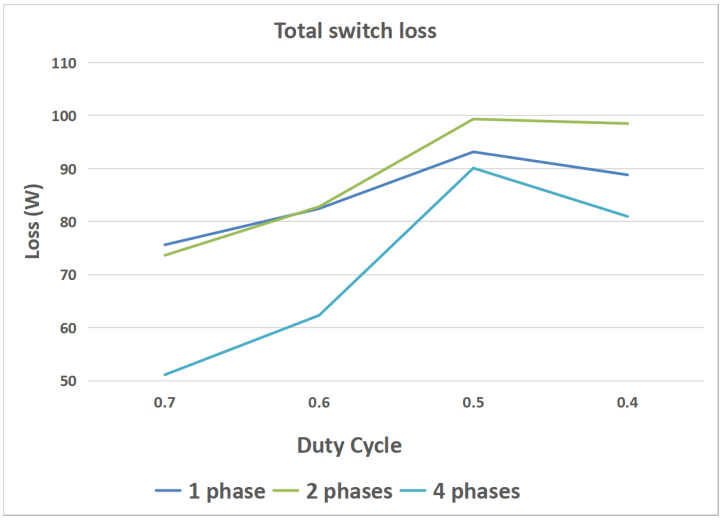

Figure 4.5: Interleaved Buck Converter Total Switch Loss Comparison under Different Duty Cycle

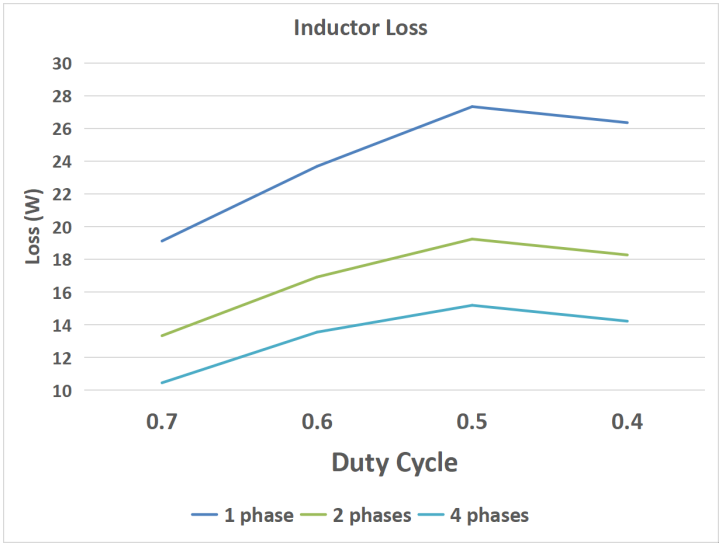

Figure 4.6: Interleaved Buck Converter Inductor Loss Comparison under Different Duty Cycle

Four conditions are taken into comparison, detailed description is shown in Table 4.2. This comparison is mainly based on considering the switch losses and the inductor losses. Thermal design and temperature are also taken into consideration for the comparison. The two variable is the number of phases and the number of inductor cores for different compare scenarios.

Table 4.2: Comparison Conditions of Interleaved Buck Converter for Topology Selection

	Number of Phases	Number of Inductor Cores
Condition A	1	1
Condition B	2	2
Condition C	2	1
Condition D	4	1

By doubling the inductor cores in one inductor, the inductor loss and temperature could be reduced as shown in Fig.4.7a and Fig.4.7b. And to compare the effect of doubling the inductor core, interleaved 2-phase buck converter topology is used. It could be seen from Fig.4.7b that doubling the inductor core promotes a significant reduction in the inductor temperature with the same thermal parameter of the heatsink used in the simulation. Fig.4.7a shows that 4-phase buck converter has the lowest inductor loss due to the low inductor current per phase. And the 4-phase buck converter's inductors also have the lowest inductor temperature, even lower than the double-core inductor with 2-phase interleaved buck topology. Although the temperature of the inductor in the 2-phase interleaved buck converter with the single core is the highest among the four conditions, the temperature rise is still within the controllable range of the thermal design. Thus, the final solution for the inductor in the interleaved buck converter will be using only one core to save cost and space.

Fig.4.7c shows that the conventional buck converter has the highest per switch loss and the 4-phase interleaved buck converter has the lowest per switch loss. But when accounting for the total switch loss of the converter, the total switch loss is calculated by the number of switches in the converter multiplied by the number of switches. Although the per switch loss in the 4-phase converter is much lower than the one in the 2-phase converter, by multiplying the number of switches, the difference is not that significant, as shown in Fig.4.7d.

Fig.4.7e shows the total loss of the converter by summing up the inductor loss times the number of inductors and the total switch loss. It could be seen from the figure that the total converter loss of the 4-phase converter is similar to the total loss in the conventional buck converter, which is much higher than the 2-phase converter, which could be explained by the high number of inductors in the 4-phase converter.

Also, because the EV charger is a commercial product, one important parameter must be taken into consideration - **cost**. Fig.4.7f shows the total cost of the switches using $C3M0065120J$. And it's easy to see from the figure that because of the number of switches in the 4-phase converter, the total switch cost almost reaches 90€. As a result, the suitable topology of the interleaved buck converter will be **an interleaved 2-phase buck converter with a single inductor core.**

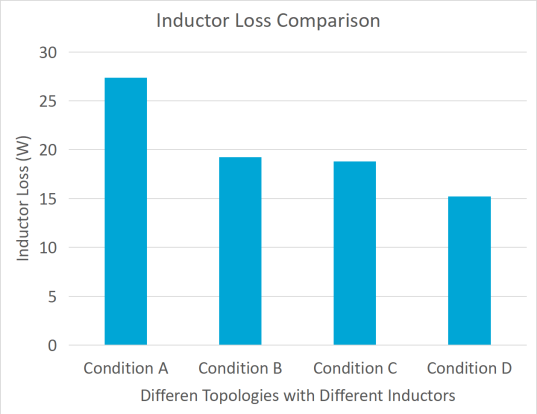

(a) Interleaved Buck Converter Inductor Loss Comparison

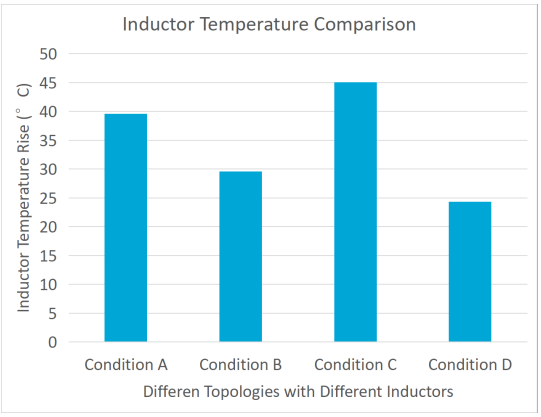

(b) Interleaved Buck Converter Inductor Temperature Comparison

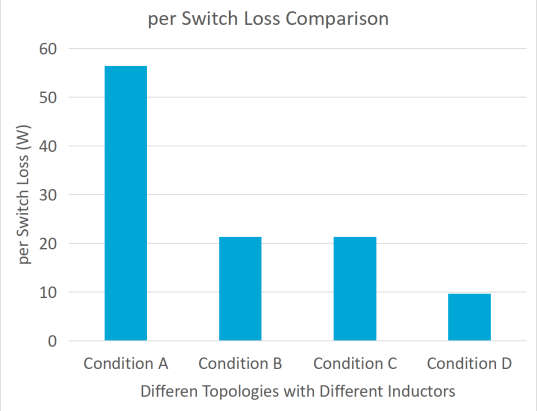

(c) Interleaved Buck Converter per Switch Loss Comparison

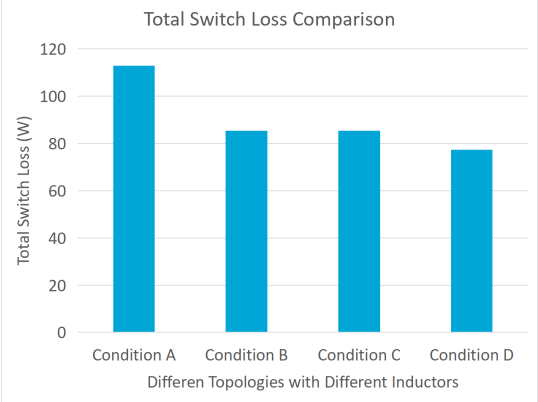

(d) Interleaved Buck Converter Total Switch Loss Comparison

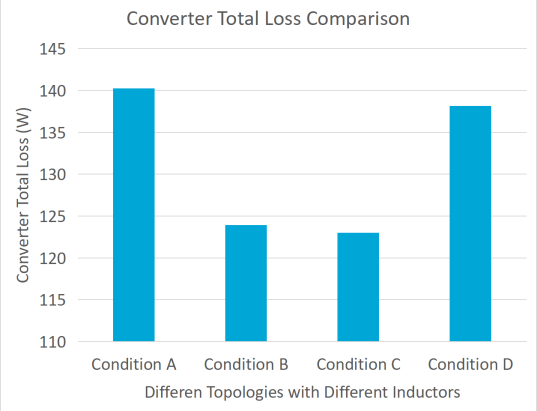

(e) Interleaved Buck Converter Total Converter Loss Comparison

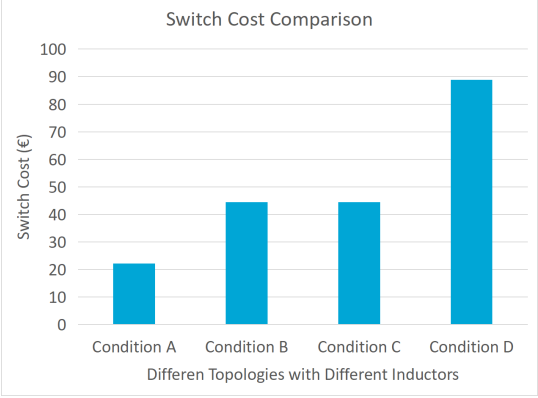

(f) Interleaved Buck Converter Switch Cost Comparison

Figure 4.7: Interleaved Buck Converter Under Different Conditions

4.2. Control Modelling

4.2.1. System Level Control Design

Fig4.8 shows how the EV charger is controlled with cascade PI controllers at a system level. The duty cycle of each interleaved buck converter is controlled by a double control loop. According to the previous section, a double control loop consists of an inner loop and an outer loop. To realize the system-level control of the EV charger, a saturation limit was added after the outer loop PI controller for different control modes. Four control modes are established for the EV charger, two charging modes and two discharging modes.

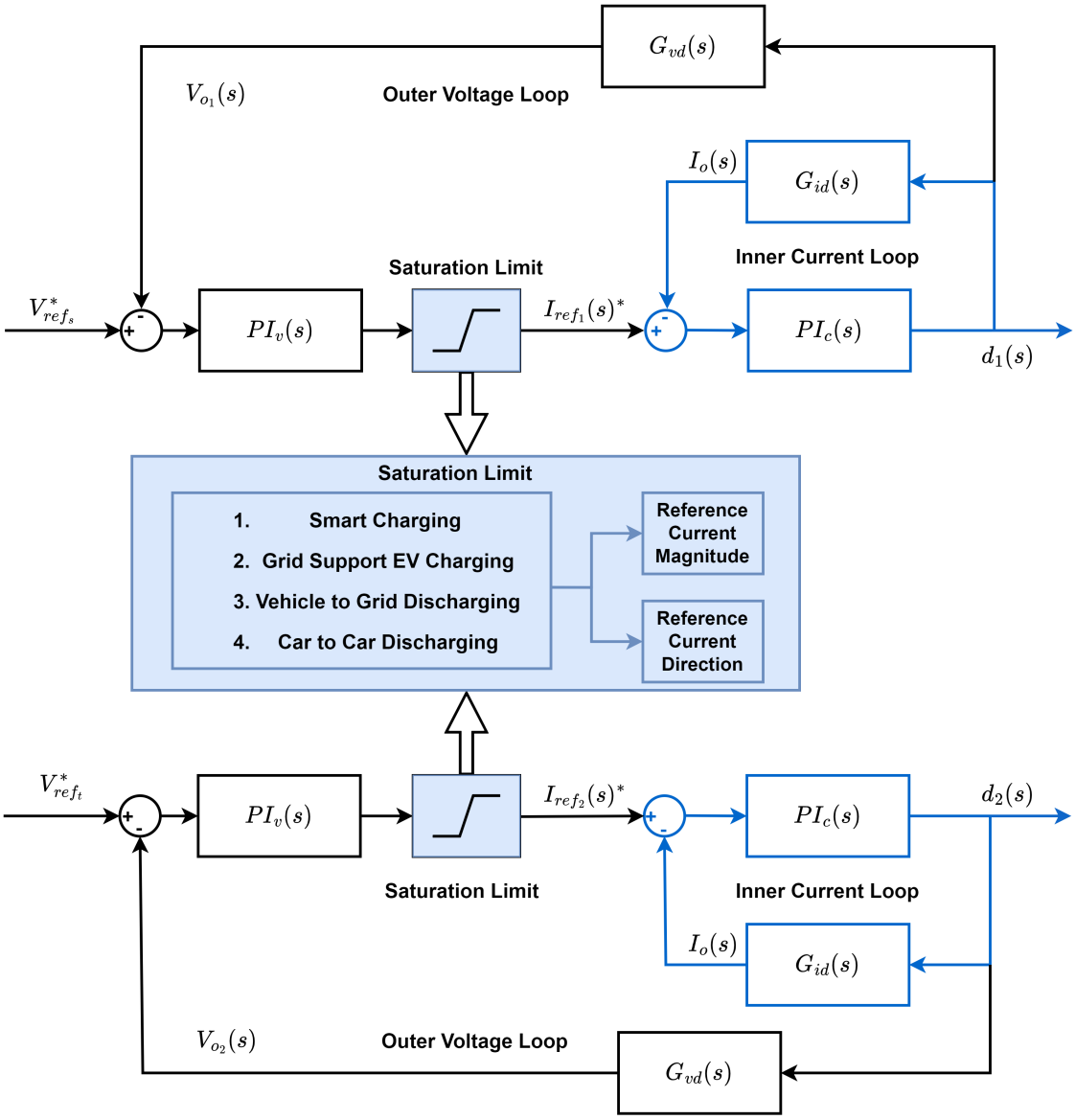

Figure 4.8: System Level Control Logic

The two charging modes are smart charging and grid-support EV charging. In the smart charging scenario, for example, if two cars with different voltage levels are connected to the EV charger to charge the battery, then the EV charger could provide unequal output power to match the different voltage levels, which is to charge the higher-voltage car with lower power and charge the low-voltage battery with higher power. Since the two interleaved buck converters are controlled by different PI controllers. And the grid support EV charging is used to help stabilize the grid with the EV battery. When the balancing converter on the grid side runs out, the EV battery can also provide support to maintain the balance of the two poles in an EV charger connected to a bipolar DC microgrid.

Fig4.9 shows the gird-support control of one pole of the grid. The blue line is the droop control of one pole of the grid and is divided into five stages. The upper limit is the grid to charge the battery at the maximum current ($375V < V_{pole} < 380V$) and the lower limit region is the battery to charge the grid at the maximum current ($340V < V_{pole} < 360V$). Any voltage beyond $380V$ and below $340V$ will stop the balancing function immediately. The upper droop ($370V < V_{pole} < 375V$) and lower droop regions ($360V < V_{pole} < 365V$) are the stages for droop control, when one pole is at this stage then the voltage will gradually approach the Idle region ($365V < V_{pole} < 370V$) with zero current flow and in the end reach the balance stage of the grid.

Detailed current charging/discharging rules are shown in Table4.3. Under most conditions, the magnitude and direction of the current is determined by the minimum current between the positive and negative pole of the grid which is decided by the droop function. The special conditions occur when one pole is charging at the edge of the upper droop region and another pole is discharging at the edge of the lower droop region because the upper droop and upper limit have higher priority so the grid will charge the battery at maximum current. Also when one pole is at the upper limit region and another is at the lower limit region, then the battery will charge the battery with maximum current. The detailed simulation result will be shown in the result chapter, as examples of the control of the EV charger by using the saturation limit.

Table 4.3: Charging and Discharging Scenarios Under Imbalanced Bipolar Grid

	Upper Limit	Upper Droop	Idle	Lower Droop	Lower Limit
Upper Limit	Minimum	Minimum	Zero	Minimum	Upper limit*
Upper Droop	Minimum	Minimum	Zero	Minimum	Minimum
Idle	Zero	Zero	Zero	Minimum	Minimum
Lower Droop	Minimum	Minimum	Minimum	Minimum	Minimum
Lower Limit	Upper limit*	Minimum	Minimum	Minimum	Minimum

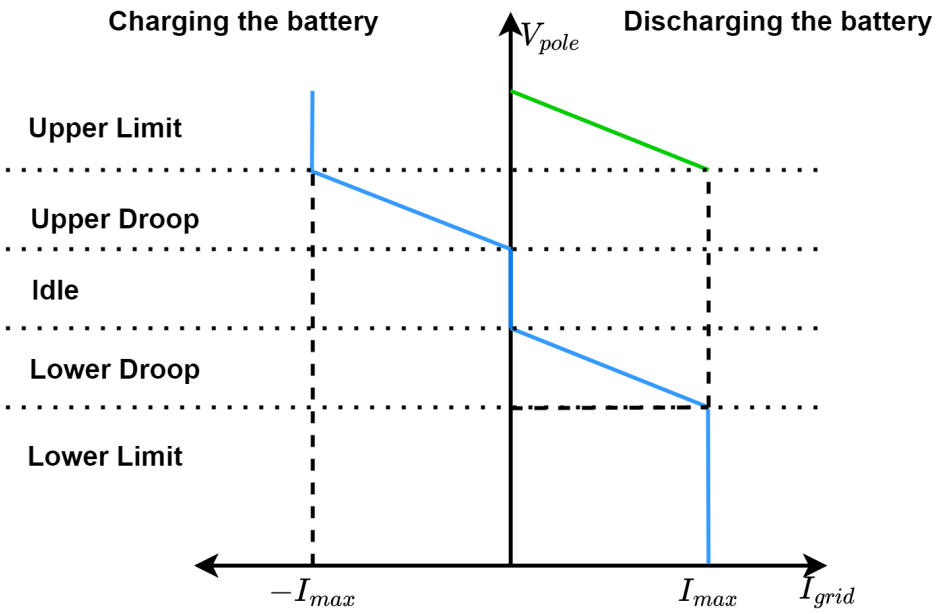

Figure 4.9: Charging and Communicating with the Grid

Correspondingly, the discharging modes consist of the vehicle-to-grid (V2G) discharging technique and the car-to-car discharging approach. In this particular context, the term ”discharging” specifically denotes the controlled release of stored energy from the EV battery. The discharging modes as shown

in Table4.4, are changed manually by the user in the EV charger UI. And the simulation result will also be shown in the result chapter.

The detailed script of realizing switching operation modes is the duty of the EV charger microcontroller, and the result of different modes are used as the saturation limit of the PI controllers. For this project, only the control of the EV charger is investigated and simulations under different scenarios are simulated and presented in the following chapter.

Also, the single output control for charging and discharging modes is stated in the state table shown in Table4.4. There are three states in total for the single output. First is when the output port is at no load condition, and then there is no switch switching, which is defined as the default plug-out state. Next is when the output port acts as load then the EV charger is in charging mode and is defined as default plug-in mode. The last state is when the output port is in source mode, then the EV charger is in discharging mode which includes car-to-car charging and vehicle-to-grid charging. The exact discharging mode will be manually determined by the user in the UI interface of the EV charger.

Table 4.4: State Table for Single Output Charging and Discharging Modes

Source	Load	No Load	Y	Description
0	0	1	No Switching	Default Plug-out
0	1	0	Charging	Default Plug-in
1	0	0	Discharging	Car-to-car Charging Vehicle-to-Grid Manually Controlled

4.2.2. Constant Frequency Control for Multiport CLLC Converter

The output voltage measurement is compared against a DC voltage set point. The error is fed into a 2-pole, 2-zero implementation of a digital PI controller as shown in Fig.4.11. An ADC interrupt is used to trigger the interrupt service routine to run the controls (simulated here as a triggered subsystem). The controls generate a counter period set point that is then converted into a frequency set point. The frequency set point is used by the PLECS variable frequency PWM block, as shown in Fig.4.10. The half-bridge FETs are switched with a 50% duty cycle. A detailed script will be included in the appendix.

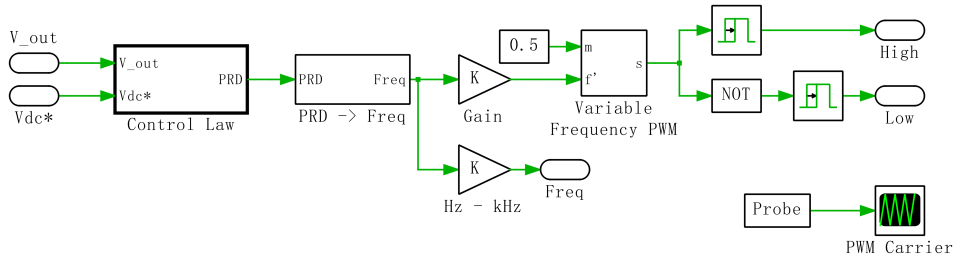

Figure 4.10: Frequency Sweep Controller for Constant Frequency Control

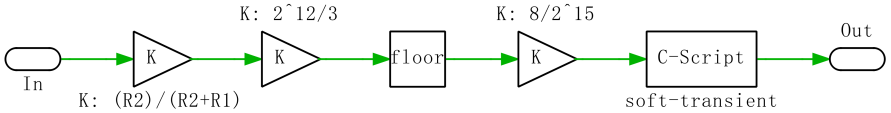

Figure 4.11: Voltage Step Controller for Constant Frequency Control

The switching frequency of the constant frequency controller's soft start and frequency sweep is

shown in Fig.4.12. The switching frequency is stepped from 660kHz to 400kHz and then to 280kHz and finally stays stable at 250kHz, with a step-down time period of $2\,ms$.

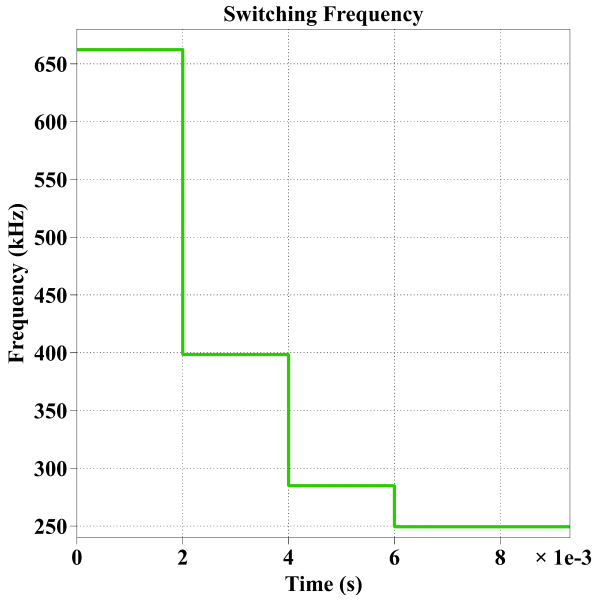

Figure 4.12: Frequency Response for CLLC

4.2.3. Double Loop Control Design for Interleaved Buck Converter

Based on the comparison result, the interleaved two-phase buck converter will be used as the solution for the voltage regulation of the EV charger by changing the duty cycle of the converter. And as stated in Section 2.2.1, linear compensators will be used with cascade loop control of the buck converter with the advantage of fast transient and zero steady-state error. This section will present a detailed design procedure of the double loop control design with a small signal model and the derivation of the interleaved buck converter.

Transfer Functions

Because the inductor currents are operating in continuous current mode (CCM), the switching averaging model could be used instead of the converter switch network [46]. The small signal model could be obtained from Fig.4.13. The output voltage V_o, output current i_t and the average duty cycle d_t are regarded as control variables.

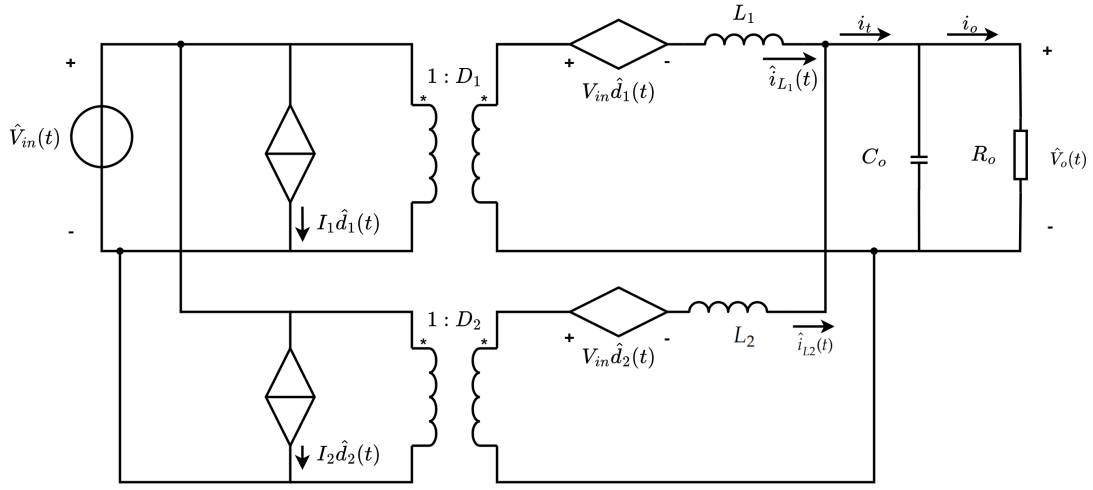

Figure 4.13: Small signal Model of Interleaved Buck Converter

From Fig.4.13, the output current i_t is the sum of the two inductor current i_{L_1} and i_{L_2}.

$$i_t = i_{L_1} + i_{L_2} \tag{4.8}$$

And the sum could be obtained as

$$i_t = \frac{1}{sL}(d_1(s)V_{in} - V_o) + \frac{1}{sL}(d_2(s)V_{in} - V_o) \tag{4.9}$$

$d_t(s)$ is the average duty cycle of the two phases. Because $d_1(s) = d_2(s)$, so

$$d_t(s) = \frac{d_1(s) + d_2(s)}{2} = d_1(s) = d_2(s) \tag{4.10}$$

The output voltage could be calculated by the RC plant transfer function and the sum current i_t as

$$V_o = i_t \frac{R_o}{R_o C s_o + 1} \tag{4.11}$$

As a result, the sum current could be calculated using the equations above:

$$\begin{aligned} i_t &= \frac{2V_{in}(R_o C_o s + 1)}{sL} d_t - \frac{2i_t \frac{R_o}{R_o C_o s + 1}}{sL} \\ &= (\frac{2V_{in}(R_o C_o s + 1)}{LR_o C_o s^2 + sL + 2R_o}) d_t \end{aligned} \tag{4.12}$$

The control loop that is used in this report is shown in Fig.2.10. So the transfer function of output current to the average duty cycle is

$$G_{id}(s) = \frac{i_t}{d_t} = \frac{2V_{in}(R_o C_o s + 1)}{R_o L C_o s^2 + sL + 2R_o} \tag{4.13}$$

And the transfer function in the outer voltage loop could be obtained as:

$$G_{vd}(s) = \frac{V_o}{d_t} = \frac{2R_o V_{in}}{R_o L C_o s^2 + Ls + 2R_o} \tag{4.14}$$

Another type of transfer function in the outer voltage loop could be deviated as :

$$G_{vi}(s) = \frac{V_o}{i_t} = \frac{R_o}{R_o C_o s + 1} \tag{4.15}$$

Fig.4.14 shows the inner control loop that is built in Simulink, where the transfer function of the PI compensator is tuned by Matlab 'sisotool'

$$C = \frac{-2.547e - 10(s - 2.109e05)}{s} \tag{4.16}$$

and G is the transfer function of $G_{id}(s)$ as shown in Eq.4.13.

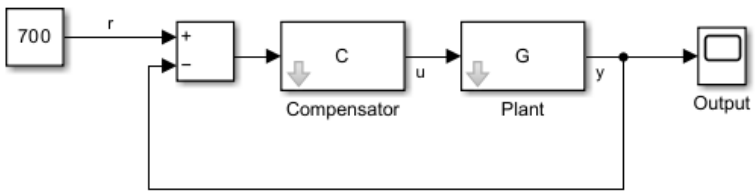

Figure 4.14: Inner Loop Schematic in Simulink

The bode plot of the PI controller shows in Fig.**??**. The gain margin of the controller is $57.9dB$ as shown in Fig.4.15 and the phase margin is $90.8°$ as shown in Fig.4.16. Both bode plots indicate that

the inner loop is a stable loop. And the step response of the loop is shown in Fig.4.17. The output result of the inner loop Simulink model is shown in Fig.4.18

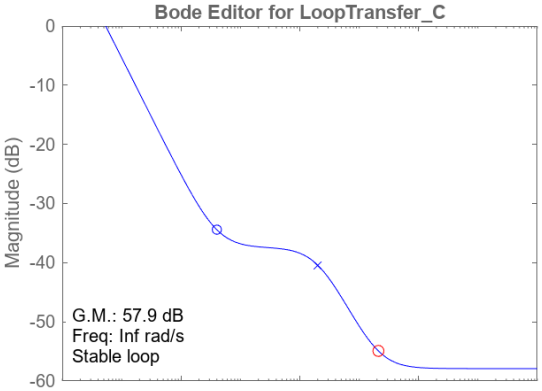

Figure 4.15: Gain Bode Plot of the inner loop

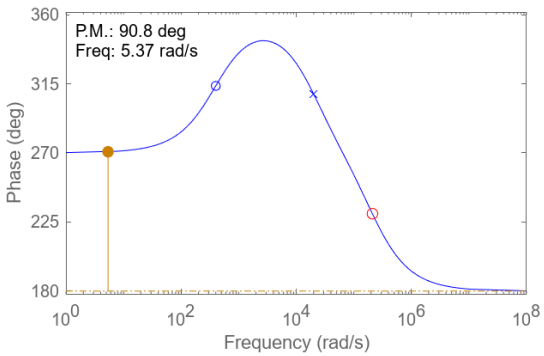

Figure 4.16: Phase Bode Plot of the inner loop

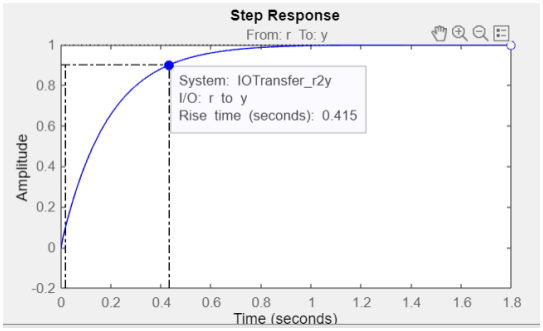

Figure 4.17: Step Response of Inner Loop

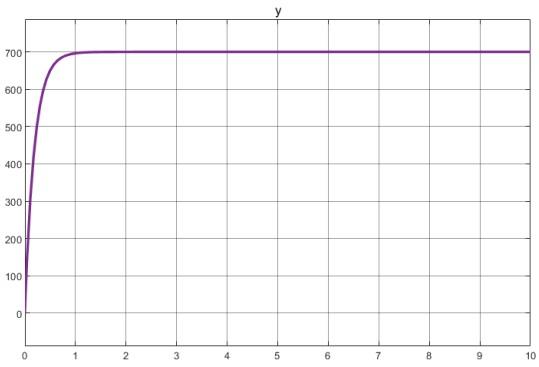

Figure 4.18: Inner Loop Simulation Result

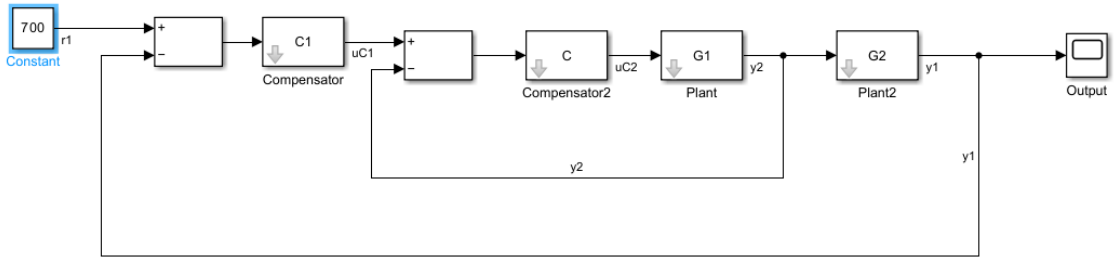

Figure 4.19: Cascade PI Control Circuit

The outer loop is built in Simulink as shown in Fig.4.19. The PI controller for the outer loop could be designed and tuned by using the Matlab 'sisotool' as:

$$C1 = \frac{1.6882(s + 14.81)}{s + 4.5} \tag{4.17}$$

The bode plot of the cascade PI controller shows in Fig.**??**. The gain margin of the controller is $67dB$ as shown in Fig.4.20 and the phase margin is $75.9°$ as shown in Fig.4.21. Both bode plots indicate that

the cascade loop is a stable loop. And the step response of the loop is shown in Fig.4.22. The output result of the inner loop Simulink model is shown in Fig.4.23

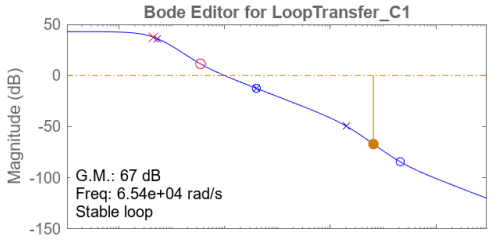

Figure 4.20: Gain Bode Plot of Cascade Loop

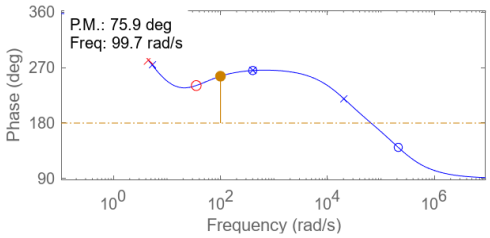

Figure 4.21: Phase Bode Plot of Cascade Loop

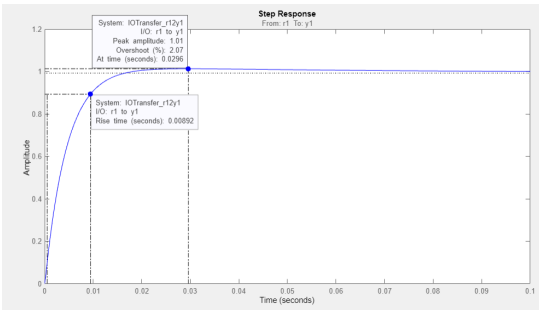

Figure 4.22: Step Response of Cascade Loop

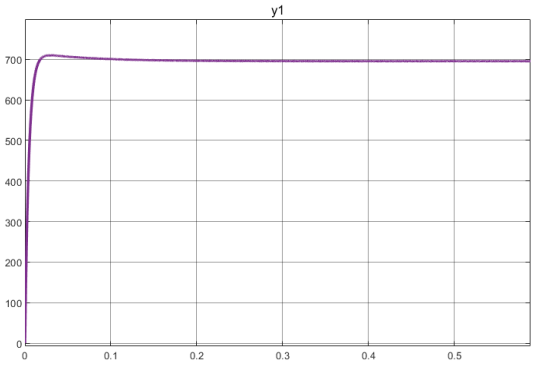

Figure 4.23: Simulation Result of Cascade Loop

5

Simulation Results and Analysis of system-level control

In this chapter, first, the schematic of the whole converter is introduced. Results of control modelling will also be presented, including simulations of car-to-car discharging and V2G discharging, simulations at different voltage levels with the same PI parameters, and one example of smart charging.

5.1. System Control Schematics

Fig.5.1 shows the schematic simulation model of the EV charger. And Fig.5.2 shows the control blocks to control the two converter topologies. The constant frequency control module is used to control the CLLC switch (S14, S23, S58 and S67), with a switching frequency that is a little beyond the corresponding resonant frequency under different circumstances. And the cascade control is used to control the gate signal in the interleaved buck converter (S1, S2, S3 and S4), with a switching frequency of 100kHz.

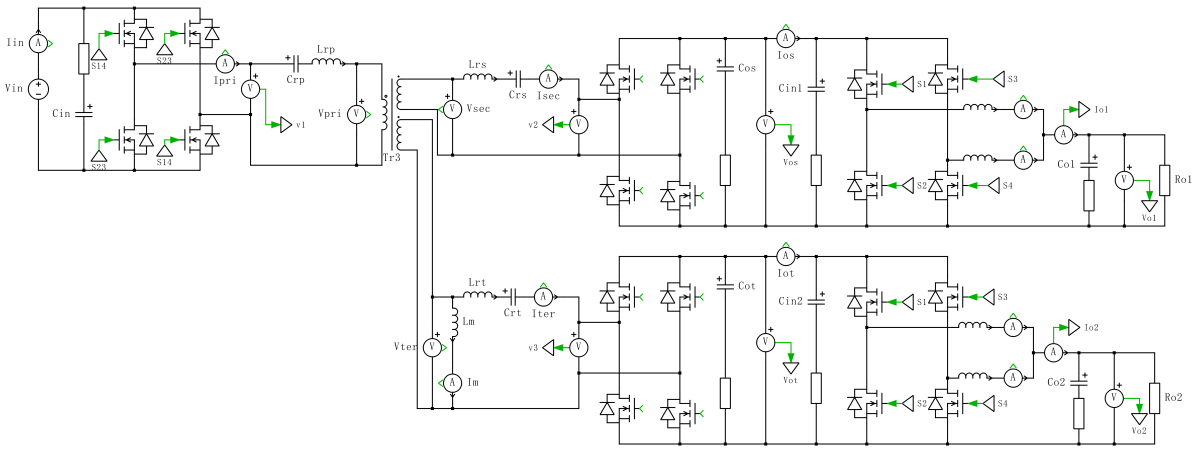

Figure 5.1: EV Charger Circuit Schematic

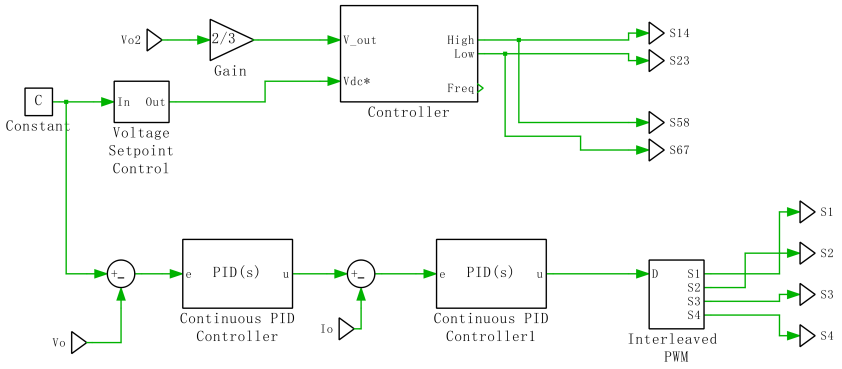

Figure 5.2: Control blocks of the EV charger

5.2. System Control Result

First of all, two different saturation limits are set for different battery voltages (400V and 700V) to verify that without adjusting the PI controller parameter, different responses are under control. Then the car-to-car charging scenario is simulated when the tertiary output is used as the input of the system and the secondary side is the real output side.

5.2.1. Cascade PI control Result

The circuit for the simulation of cascade PI control is shown in Fig.5.3. As introduced before, there are two operation modes for the interleaved buck converter, maximum current and maximum power. Reintroducing the operation modes briefly, when the battery voltage is higher than 550V, the control will operate under maximum power (11kW) by setting the saturation limit to be the calculated value based on the fixed power and the battery voltage. When the battery voltage is lower than 550V, the control will operate under maximum current mode (20A), and then the saturation limit will be set to 20A.

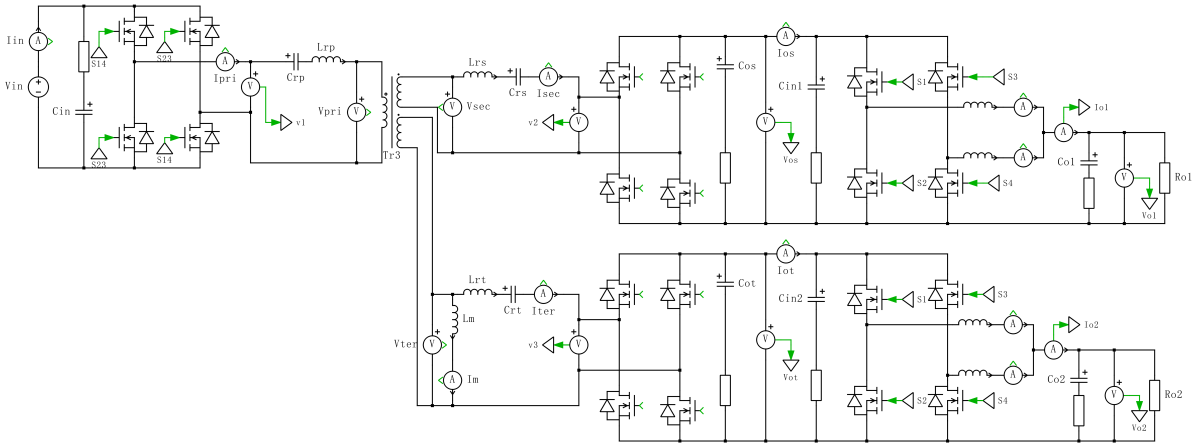

Figure 5.3: Circuit Schematic for Cascade PI Control Simulations

Fig.5.4 shows the simulation result of the duty cycle, output current and output voltage when the battery voltage is 400V which is under maximum current working mode. Fig.5.5 shows the simulation result of the duty cycle, output current and output voltage when the battery voltage is 7400V which is under maximum power working mode. And it could be seen from both figures that the controlled output has a low variation and a fast response. And the ripples of the duty cycle decrease when the battery voltage increases. Overall the system response has a reasonable performance which indicates that the PI controller parameters are well-tuned.

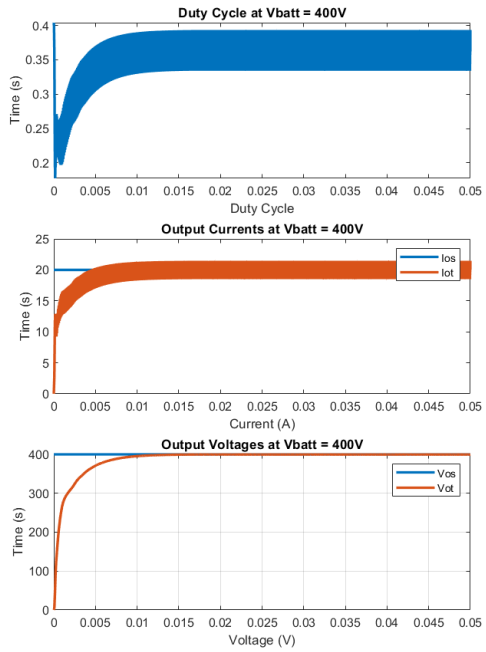

Figure 5.4: EV Charger Performances when $V_{batt} = 400V$

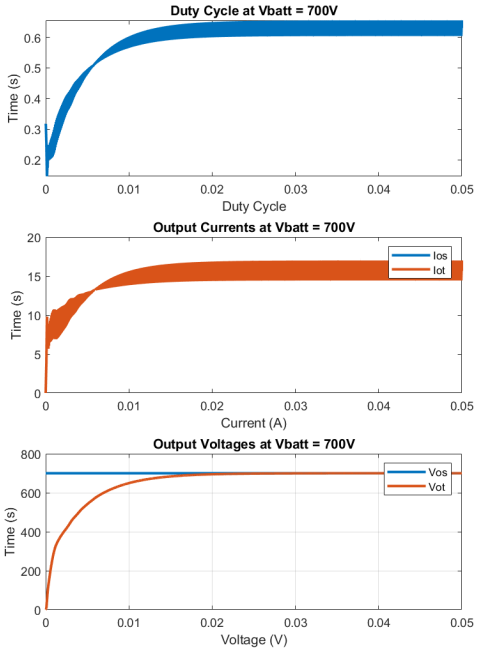

Figure 5.5: EV Charger Performances when $V_{batt} = 700V$

5.2.2. Car-to-car Discharging

Fig.5.6 shows the circuit schematic of the car-to-car charging scenario. The tertiary side of the CLLC converter is used as the input and the secondary side is treated with a load to simulate the car-to-car charging operation. Only the tertiary switches are actively switched to control the power flow. The grid voltage is set to 700V and the tertiary voltage is set to 1100V.

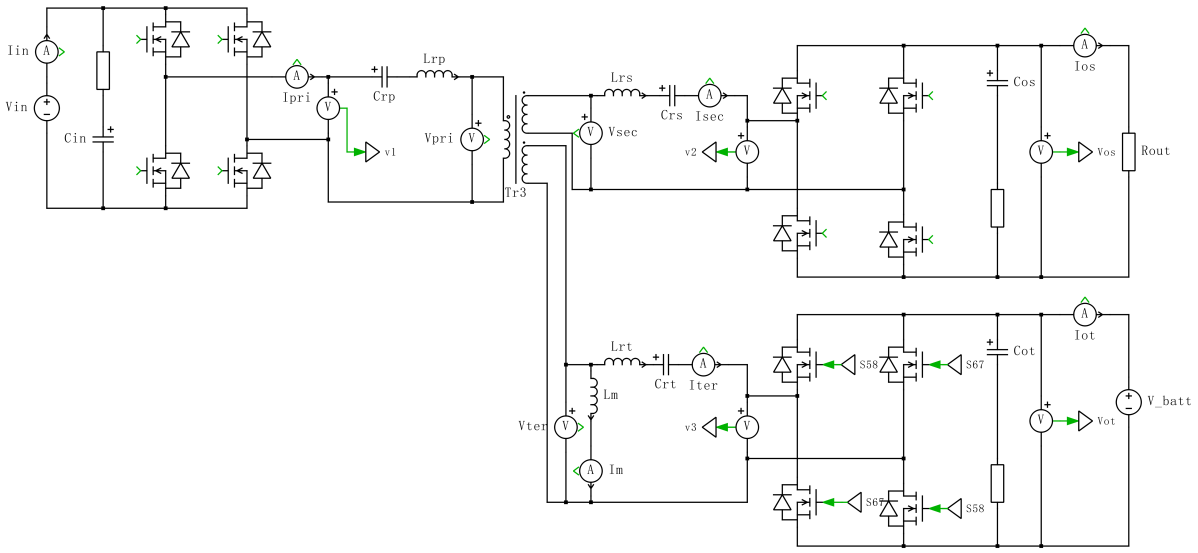

Figure 5.6: Circuit Schematic for Car-to-car Discharging Simulations

And the car-to-car charging simulation results are shown below. Fig.5.7 shows the voltage and current response of the converter and Fig.5.8 shows the power flow in the three ports. It could be seen from the figure that the primary voltage of the transformer is higher than the gird voltage so that

the power flowing through the primary side is zero. And the resonant frequency is recalculated to be 400kHz. The car-to-car charging is well realized in the simulation.

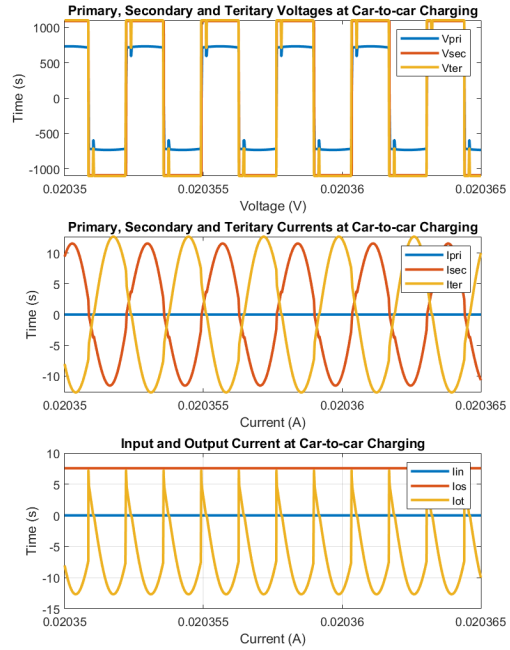

Figure 5.7: EV Charger Voltage and Current Performances at car-to-car charging

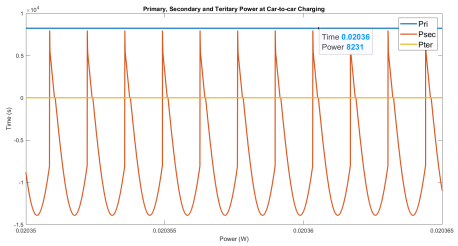

Figure 5.8: EV Charger Power Performances at car-to-car charging

5.2.3. Vehicle to Grid Discharging

Fig.5.9 shows the circuit schematic of the vehicle-to-grid charging scenario. The tertiary and secondary sides of the CLLC converter are used as the input and the primary side is treated with a load to simulate the vehicle-to-grid charging operation. Both the tertiary and secondary switches are actively switched to control the inverted power flow. The grid load is set to 733.33V and the tertiary voltage is set to 1100V.

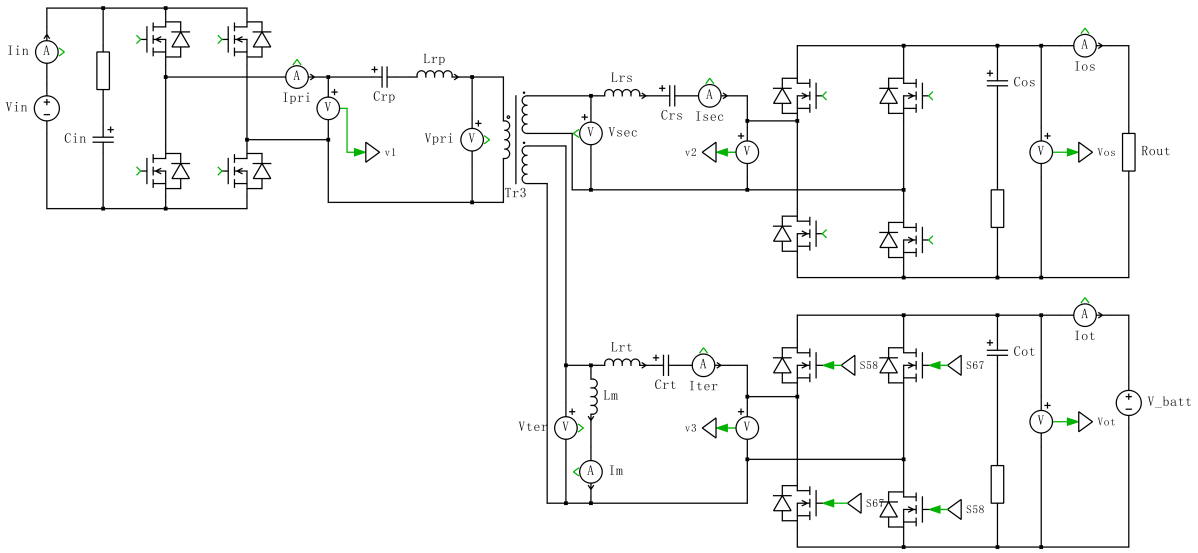

Figure 5.9: Circuit Schematic for Vehicle-to-Grid Discharging Simulations

And the vehicle-to-grid charging simulation results are shown below. Fig.5.10 shows the voltage and current response of the converter and Fig.5.8 shows the power flow in the three ports. It could be seen from the figure. The current flowing through the tertiary side is negative which could be explained by the ammeter current shown in Fig.5.9 The vehicle-to-grid charging is well realized in the simulation, which shows that the EV charge r has bidirectionality and has the ability to help support the grid.

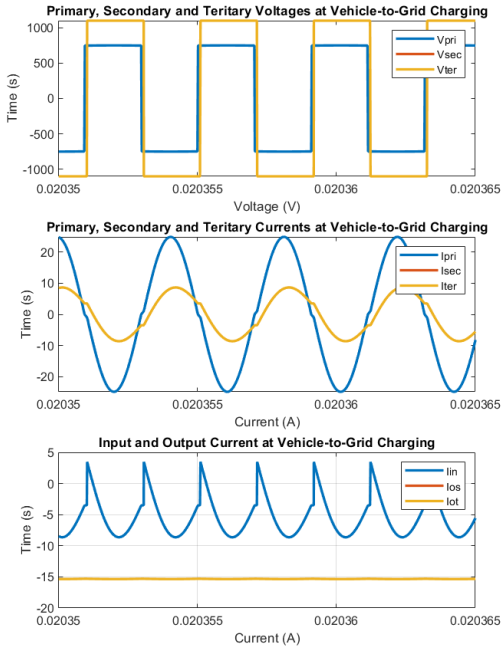

Figure 5.10: EV Charger Voltage and Current Performances at Vehicle-to-Grid Charging

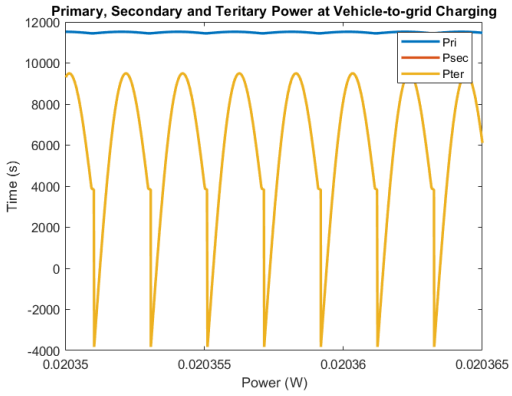

Figure 5.11: EV Charger Power Performances at Vehicle-to-Grid Charging

5.2.4. Smart Charging

Unequal output power simulation is presented as an example of smart charging. Assume that there's a condition that the two cars connected to the EV charger have different voltage levels. Then the EV charger should charge the higher voltage battery with lower power and charge the lower voltage battery with higher power. In the simulation, the interleaved buck converter connected on the secondary side is charged with maximum current on 20A and an output power of 3kW is obtained by the load. Another output load with a battery voltage of 400V is charged at 8kW. The two interleaved buck converters are controlled by separate cascade PI control loops and the saturation limits in each control loop are determined based on the battery voltage and control modes.

The results are shown below. Fig.5.12 shows output power and the PI-controlled output current of the two output ports. It could be seen from the figure that the output current ripples have similar values which shows the well-tuned PI parameters could control the output current with different inputs. Fig.5.13 shows the duty cycle under two different charging modes of the EV charger. And it could be seen from the figure that due to the difference in the battery voltage, the duty cycles have different values and inverted slopes.

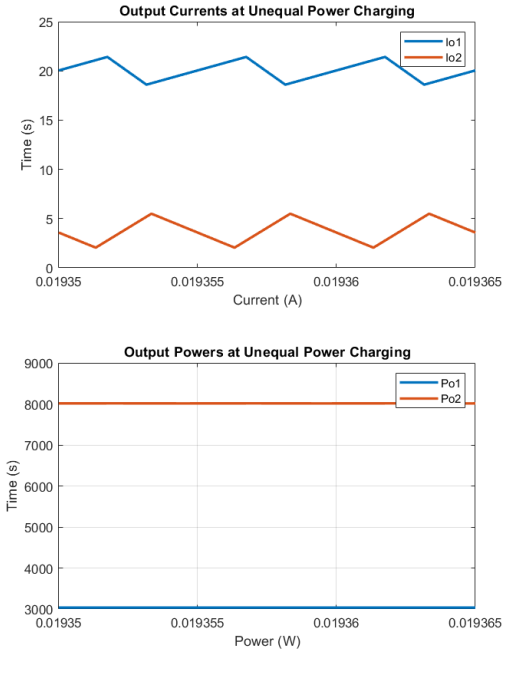

Figure 5.12: Interleaved Buck Converter Output Current and Power at Unequal Power Charging

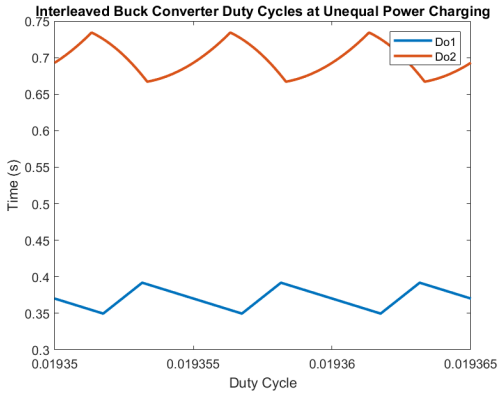

Figure 5.13: Interleaved Buck Converter Duty Cycles at Unequal Power Charging

5.2.5. Grid Droop Control Charging

Fig.5.14 shows the same control function as Fig.4.9 introduced before but with detailed voltage specifications. Here, one specific condition is simulated to demonstrate the ability of the EV charger to support grids.

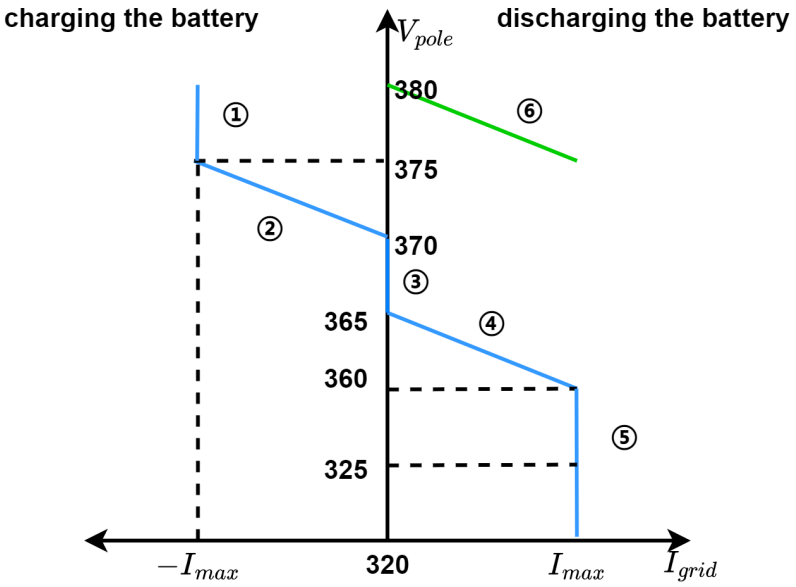

Figure 5.14: Grid-Droop Control with Detailed Parameters

When the positive pole of the bipolar grid is $375V$ and the negative pole voltage of the grid is $372V$, the grid current should following the minimum current comparing between the two poles, which means

the current at $372V$. When the $V_{pole} \in (370V, 375V)$, the grid current could be calculated using the equations below and the result is shown below.

$$\begin{aligned} I_{grid} &= 2.894 \times V_{pole} - 1069.18 \\ I_{grid} &= 7.388\ A \end{aligned} \tag{5.1}$$

With the calculated grid current, the input power that is supplied by the grid is obtained to calculate the amount of power that could be transferred to the vehicle. Assuming the battery voltage is $400V$, the EV charger should charge the car with maximum current (20A) in the normal charging mode. However, because the EV battery is used to support the grid stability, the power transfered to the battery is reduced and the output current of the interleaved buck converter is determined by the total amount of power provided by the grid.

Fig.5.15 shows the controlled duty cycle as the final output of the PI control loop and Fig5.16 shows the controlled output current and the calculated saturation limit under the grid-droop condition. It could be seen from the figures that even though the operation modes changed and the saturation limit changed, the tuned PI parameters could also support the control with fast response.

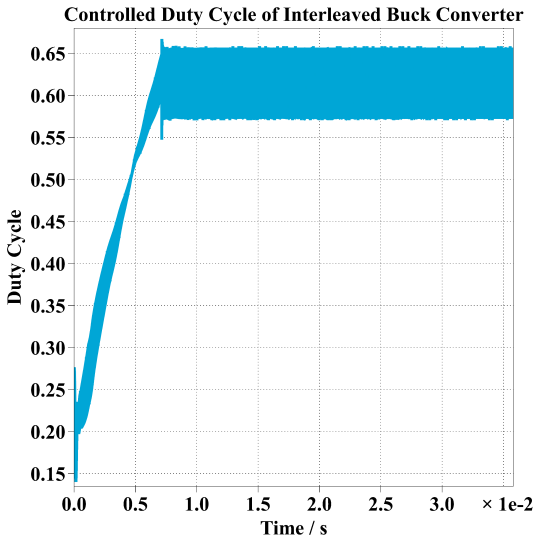

Figure 5.15: Output Current of the EV Charger with Grid-Droop Operation

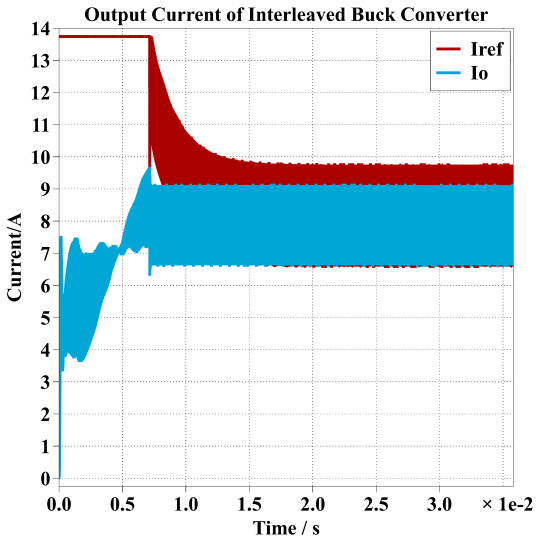

Figure 5.16: Controlled Duty Cycle of the EV Charger with Grid-Droop Operation

6 Conclusion

6.1. Answering Research Questions

What are the suitable topologies for a bidirectional isolated dual-output EV charger connected between a DC microgrid and considering a wide output voltage range of EV batteries?

For the single-output isolated converter, LLC is not suitable for the EV charger because it cannot work in the reverse power flow mode. Comparing CLLC and DAB converters, DAB has the risk that it might lose ZVS at light load, whereas CLLC could maintain ZVS at the whole load range but with a higher conduction loss. The dual-output converter has the advantage of saving switches on the primary side, compared with using two identical single-output converters, which contributes to the high efficiency and low cost. Then multiport CLLC converter and TAB are more suitable than normal CLLC converter and DAB.

What is the outcome of a comparative analysis between the Triple Active Bridge and Multiport CLLC converter for the dual-output EV charger converter application?

While the TAB converter has a lower conduction loss and a wide voltage gain and ZVS range, the complex phase shift control and decoupling control add to the complexity of the EV charger control. In addition, although the resonant frequency of the multiport CLLC converter might change in real life, CLLC converters are easier to control than TAB converters. In addition to the ability to operate with open-loop control, the multiport CLLC converter could act as an ideal DC transformer for power transfer.

How can a simplified open-loop control strategy be implemented for the CLLC while maintaining ZVS over the entire input voltage range of the DC grid?

When operating at a fixed resonant frequency, the multiport CLLC converter could act as an ideal DC transformer. With the designed transformer turns ratio, the output voltage is always above 1000V. Using interleaved buck converter, the output voltage of the EV charger could support a wide range from 200V to 920V by controlling the duty cycle. A cascade PI control is implemented on the interleaved buck converter to control the output voltage.

How to model and design the control for the EV charger converter and simulate the control across various scenarios, including load changes, power flow changes, and grid variations?

By controlling the saturation limit of the PI controller in the voltage loop of the cascade PI control loop of the interleaved buck converter, a system-level control for the EV charger is presented. An unequal output power condition is simulated as an example of the smart charging for the load changes. Car-to-car charging and vehicle-to-grid charging are also modelled and simulated. Finally, a grid-droop control simulation is presented for the grid variation change scenarios.

6.2. Recommendations

For the cascade PI control, the parameters of the PI controller are tuned under high-power conditions, it could be tuned again under low-power conditions to reduce the output current ripple seen in the droop control condition which has a relatively low power flow.

Also, since this thesis only focuses on the simulation and control design, a further design in the hardware would be nice to test the EV charger design in real life and even test the converter with the designed control in connection with the real DC microgrid.

Planar transformers are another recommendation for the hardware design. For the EV charger, only the transformer's turns ratio and some other parameters have been designed. The design of a multiport CLLC converter with two output windings and integrated inductors could also prove challenging.

Final recommendation will be the passive cooling method, some loss calculations and rough heatsink design are conducted in this project, but detailed heatsink design is not derived. It is also interesting to observe if passive cooling is enough for this EV charger and what kind of heatsink is needed for the heat dissipation.

References

[1] Tomislav Dragičević et al. “DC microgrids—Part II: A review of power architectures, applications, and standardization issues”. In: *IEEE transactions on power electronics* 31.5 (2015), pp. 3528–3549.

[2] Sachpreet Kaur et al. “A state of the art of DC microgrids for electric vehicle charging”. In: *2017 4th International Conference on Signal Processing, Computing and Control (ISPCC)*. IEEE. 2017, pp. 381–386.

[3] Hossein Lotfi and Amin Khodaei. “AC versus DC microgrid planning”. In: *IEEE Transactions on Smart Grid* 8.1 (2015), pp. 296–304.

[4] Dominic A Savio et al. “Photovoltaic integrated hybrid microgrid structured electric vehicle charging station and its energy management approach”. In: *Energies* 12.1 (2019), p. 168.

[5] IEA. *Electric Vehicles*. License: CC BY 4.0. IEA, 2022. URL: https://www.iea.org/reports/electric-vehicles.

[6] IEA. *Global EV Outlook 2022*. License: CC BY 4.0. IEA, 2022. URL: https://www.iea.org/reports/global-ev-outlook-2022.

[7] IEA. *Slow publicly available chargers, 2015-2021*. IEA, Paris. IEA. Licence: CC BY 4.0. 2021. URL: https://www.iea.org/data-and-statistics/charts/slow-publicly-available-chargers-2015-2021.

[8] Sang Chon, Manish Bhardwaj, and Hrishi Nene. “Maximizing power for Level 3 EV charging stations”. In: *Texas Instrument Article* (2018), pp. 1–33.

[9] Hongmei Wan. “High efficiency DC-DC converter for EV battery charger using hybrid resonant and PWM technique”. PhD thesis. Virginia Tech, 2012.

[10] Mena ElMenshawy and Ahmed Massoud. “Medium-Voltage DC-DC Converter Topologies for Electric Bus Fast Charging Stations: State-of-the-Art Review”. In: *Energies* 15.15 (2022), p. 5487.

[11] Jee-Hoon Jung et al. “Design methodology of bidirectional CLLC resonant converter for high-frequency isolation of DC distribution systems”. In: *IEEE Transactions on Power Electronics* 28.4 (2012), pp. 1741–1755.

[12] Shishuo Zhao. “High frequency isolated power conversion from medium voltage AC to low voltage DC”. PhD thesis. Virginia Tech, 2017.

[13] Liqiang Yuan et al. “Comparative evaluation of isolated bidirectional DC/DC converter in high-power high-frequency occasions”. In: *2018 21st International Conference on Electrical Machines and Systems (ICEMS)*. IEEE. 2018, pp. 2285–2290.

[14] Kevin Tomas-Manez, Zhe Zhang, and Ziwei Ouyang. “Multi-port isolated LLC resonant converter for distributed energy generation with energy storage”. In: *2017 IEEE Energy Conversion Congress and Exposition (ECCE)*. IEEE. 2017, pp. 2219–2226.

[15] Peiwen He and Alireza Khaligh. “Comprehensive analyses and comparison of 1 kW isolated DC–DC converters for bidirectional EV charging systems”. In: *IEEE Transactions on Transportation electrification* 3.1 (2016), pp. 147–156.

[16] Chunjiang Zhang et al. “Integrated half-bridge CLLC bidirectional converter for energy storage systems”. In: *IEEE Transactions on Industrial Electronics* 65.5 (2017), pp. 3879–3889.

[17] Jun Min and Martin Ordonez. “Bidirectional resonant CLLC charger for wide battery voltage range: Asymmetric parameters methodology”. In: *IEEE Transactions on Power Electronics* 36.6 (2020), pp. 6662–6673.

[18] Levon Gevorkov et al. “Modern MultiPort Converter Technologies: A Systematic Review”. In: *Applied Sciences* 13.4 (2023), p. 2579.

[19] Pavel Purgat et al. “Zero voltage switching criteria of triple active bridge converter”. In: *IEEE Transactions on Power Electronics* 36.5 (2020), pp. 5425–5439.

[20] Pavel Purgat et al. “Power Flow Decoupling Controller for Triple Active Bridge Based on Fourier Decomposition of Transformer Currents”. In: *2020 IEEE Applied Power Electronics Conference and Exposition (APEC)*. IEEE. 2020, pp. 1201–1208.

[21] Shenli Zou, Jiangheng Lu, and Alireza Khaligh. “Modelling and control of a triple-active-bridge converter”. In: *IET Power Electronics* 13.5 (2020), pp. 961–969.

[22] Ishita Biswas, Debaprasad Kastha, and Prabodh Bajpai. “Small signal modeling and decoupled controller design for a triple active bridge multiport DC–DC converter”. In: *IEEE Transactions on Power Electronics* 36.2 (2020), pp. 1856–1869.

[23] Ashwin Chandwani, Ayan Mallik, and Arunachala Mada Kannan. “A novel decoupled control scheme for phase controlled triple active bridge”. In: *IECON 2021–47th Annual Conference of the IEEE Industrial Electronics Society*. IEEE. 2021, pp. 1–6.

[24] Soumya Bandyopadhyay et al. “A multiactive bridge converter with inherently decoupled power flows”. In: *IEEE Transactions on Power Electronics* 36.2 (2020), pp. 2231–2245.

[25] Yan-Kim Tran, Dražen Dujić, and Philippe Barrade. “Multiport resonant DC-DC converter”. In: *IECON 2015-41st Annual Conference of the IEEE Industrial Electronics Society*. IEEE. 2015, pp. 003839–003844.

[26] Yan-Kim Tran and Drazen Dujic. “A multiport isolated DC-DC converter”. In: *2016 IEEE Applied Power Electronics Conference and Exposition (APEC)*. IEEE. 2016, pp. 156–162.

[27] Xiang Lin et al. “A multi-port bidirectional power conversion system for reversible solid oxide fuel cell applications”. In: *2018 International Power Electronics Conference (IPEC-Niigata 2018-ECCE Asia)*. IEEE. 2018, pp. 3460–3465.

[28] Zoran Pavlović et al. “Bidirectional multiple port dc/dc transformer based on a series resonant converter”. In: *2013 Twenty-Eighth Annual IEEE Applied Power Electronics Conference and Exposition (APEC)*. IEEE. 2013, pp. 1075–1082.

[29] Stefania Cuoghi et al. “Multileg interleaved buck converter for EV charging: Discrete-time model and direct control design”. In: *Energies* 13.2 (2020), p. 466.

[30] Jong-Pil Lee et al. “Analysis and design of coupled inductors for two-phase interleaved DC-DC converters”. In: *Journal of power electronics* 13.3 (2013), pp. 339–348.

[31] S Vijayalakshmi, E Arthika, and G Shanmuga Priya. “Modeling and simulation of interleaved Buck-boost converter with PID controller”. In: *2015 IEEE 9th International Conference on Intelligent Systems and Control (ISCO)*. IEEE. 2015, pp. 1–6.

[32] Mario Norman Syah, Eka Firmansyah, and Dzuhri Radityo Utomo. “Interleaved Bidirectional DC-DC Converter Operation Strategies and Problem Challenges: An Overview”. In: *2022 IEEE International Conference in Power Engineering Application (ICPEA)*. IEEE. 2022, pp. 1–6.

[33] Xinchen Wang, Enrong Wang, and Hailong Zhang. “Design of improved double closed-loop controlled interleaved parallel buck circuit”. In: *2017 International Conference on Advanced Mechatronic Systems (ICAMechS)*. IEEE. 2017, pp. 224–229.

[34] F Liccardo et al. “Interleaved dc-dc converters for photovoltaic modules”. In: *2007 International Conference on Clean Electrical Power*. IEEE. 2007, pp. 201–207.

[35] Rammohan Rao Makineni et al. “Dual Loop Cascade Control of a Stacked Interleaved Buck Converter for Electrolyzer Application”. In: *2022 IEEE IAS Global Conference on Emerging Technologies (GlobConET)*. IEEE. 2022, pp. 1029–1035.

[36] Mohammad Hazzaz Mahmud and Yue Zhao. “Sliding mode duty cycle control with current balancing algorithm for an interleaved buck converter-based PV source simulator”. In: *IET Power Electronics* 11.13 (2018), pp. 2117–2124.

[37] Siew-Chong Tan, Yuk-Ming Lai, and Chi K Tse. “A unified approach to the design of PWM-based sliding-mode voltage controllers for basic DC-DC converters in continuous conduction mode”. In: *IEEE Transactions on Circuits and Systems I: Regular Papers* 53.8 (2006), pp. 1816–1827.

[38] Yue Zhao, Wei Qiao, and Daihyun Ha. “A sliding-mode duty-ratio controller for DC/DC buck converters with constant power loads”. In: *IEEE Transactions on industry Applications* 50.2 (2013), pp. 1448–1458.

[39] Babak Rahrovi, Ramin Tafazzoli Mehrjardi, and Mehrdad Ehsani. “On the analysis and design of high-frequency transformers for dual and triple active bridge converters in more electric aircraft”. In: *2021 IEEE Texas Power and Energy Conference (TPEC)*. IEEE. 2021, pp. 1–6.

[40] Chuanhong Zhao, Simon D Round, and Johann W Kolar. “An isolated three-port bidirectional DC-DC converter with decoupled power flow management”. In: *IEEE transactions on power electronics* 23.5 (2008), pp. 2443–2453.

[41] Sangtaek Han, Imayavaramban Munuswamy, and Deepak Divan. “Preventing transformer saturation in bi-directional dual active bridge buck-boost DC/DC converters”. In: *2010 IEEE Energy Conversion Congress and Exposition*. IEEE. 2010, pp. 1450–1457.

[42] G Ortiz et al. “Application of the magnetic ear for flux balancing of a 160kW/20kHz DC-DC converter transformer”. In: *2013 Twenty-Eighth Annual IEEE Applied Power Electronics Conference and Exposition (APEC)*. IEEE. 2013, pp. 2118–2124.

[43] Zian Qin et al. “A dual active bridge converter with an extended high-efficiency range by DC blocking capacitor voltage control”. In: *IEEE Transactions on Power Electronics* 33.7 (2017), pp. 5949–5966.

[44] Peng Liu and Shanxu Duan. “A hybrid modulation strategy providing lower inductor current for the DAB converter with the aid of DC blocking capacitors”. In: *IEEE Transactions on Power Electronics* 35.4 (2019), pp. 4309–4320.

[45] Eun-Soo Kim and Jae-Sung Oh. “High-Efficiency Bidirectional LLC Resonant Converter with Primary Auxiliary Windings”. In: *Energies* 12.24 (2019). ISSN: 1996-1073. DOI: 10.3390/en12244692. URL: https://www.mdpi.com/1996-1073/12/24/4692.

[46] Wenhao Hu et al. “Decoupled average current balancing method for interleaved buck converters with dual closed-loop control”. In: *2020 IEEE 9th International Power Electronics and Motion Control Conference (IPEMC2020-ECCE Asia)*. IEEE. 2020, pp. 578–583.